

AFRL-AFOSR-UK-TR-2012-0019



Effects of passive porous walls on the first mode of hypersonic boundary layers over a sharp cone

Dr. Sharon O. Stephen

**University of Birmingham
School of Mathematics
Edgbaston
Birmingham, United Kingdom B15 2TT**

EOARD Grant 08-3044

Report Date: December 2011

Final Report for 15 October 2008 to 14 October 2011

Distribution Statement A: Approved for public release distribution is unlimited.

**Air Force Research Laboratory
Air Force Office of Scientific Research
European Office of Aerospace Research and Development
Unit 4515 Box 14, APO AE 09421**

REPORT DOCUMENTATION PAGE				Form Approved OMB No. 0704-0188	
<p>Public reporting burden for this collection of information is estimated to average 1 hour per response, including the time for reviewing instructions, searching existing data sources, gathering and maintaining the data needed, and completing and reviewing the collection of information. Send comments regarding this burden estimate or any other aspect of this collection of information, including suggestions for reducing the burden, to Department of Defense, Washington Headquarters Services, Directorate for Information Operations and Reports (0704-0188), 1215 Jefferson Davis Highway, Suite 1204, Arlington, VA 22202-4302. Respondents should be aware that notwithstanding any other provision of law, no person shall be subject to any penalty for failing to comply with a collection of information if it does not display a currently valid OMB control number.</p> <p>PLEASE DO NOT RETURN YOUR FORM TO THE ABOVE ADDRESS.</p>					
1. REPORT DATE (DD-MM-YYYY) 9 December 2011		2. REPORT TYPE Final Report		3. DATES COVERED (From – To) 15 October 2008 – 14 October 2011	
4. TITLE AND SUBTITLE Effects of passive porous walls on the first mode of hypersonic boundary layers over a sharp cone			5a. CONTRACT NUMBER FA8655-08-1-3044		
			5b. GRANT NUMBER Grant 08-3044		
			5c. PROGRAM ELEMENT NUMBER 61102F		
			5d. PROJECT NUMBER		
6. AUTHOR(S) Dr. Sharon O. Stephen			5d. TASK NUMBER		
			5e. WORK UNIT NUMBER		
7. PERFORMING ORGANIZATION NAME(S) AND ADDRESS(ES) University of Birmingham School of Mathematics Edgbaston Birmingham, United Kingdom B15 2TT			8. PERFORMING ORGANIZATION REPORT NUMBER N/A		
9. SPONSORING/MONITORING AGENCY NAME(S) AND ADDRESS(ES) EOARD Unit 4515 BOX 14 APO AE 09421			10. SPONSOR/MONITOR'S ACRONYM(S) AFRL/AFOSR/RSW (EOARD)		
			11. SPONSOR/MONITOR'S REPORT NUMBER(S) AFRL-AFOSR-UK-TR-2012-0019		
12. DISTRIBUTION/AVAILABILITY STATEMENT Approved for public release; distribution is unlimited.					
13. SUPPLEMENTARY NOTES					
14. ABSTRACT A theoretical linear stability analysis is used to consider the effect of a porous wall on the first mode of a hypersonic boundary layer on a sharp slender cone. The effects of curvature and of the attached shock are included for axisymmetric and non-axisymmetric disturbances. The flow in the hypersonic boundary layer is coupled to the flow in the porous layer. The linear results for neutral stability and spatial stability are presented for physical parameters and porous wall models, chosen to correspond to relevant experiments. The effects of varying the porous wall parameters are investigated. A weakly nonlinear stability analysis is carried out allowing an equation for the amplitude of disturbances to be derived. The coefficients of the terms in the amplitude equation are evaluated for axisymmetric and non-axisymmetric disturbances. The stabilizing or destabilizing effect of nonlinearity is found to depend on the cone radius. The presence of porous walls significantly influences the effect of nonlinearity.					
15. SUBJECT TERMS EOARD, Mathematics, Hypersonics					
16. SECURITY CLASSIFICATION OF:			17. LIMITATION OF ABSTRACT SAR	18. NUMBER OF PAGES 54	19a. NAME OF RESPONSIBLE PERSON Gregg Abate
a. REPORT UNCLAS	b. ABSTRACT UNCLAS	c. THIS PAGE UNCLAS			19b. TELEPHONE NUMBER (Include area code) +44 (0)1895 616021

Effects of passive porous walls on the first mode of hypersonic boundary layers over a sharp cone

Principal investigator: Sharon O. Stephen,
Ph.D. student: Vipin Michael,
School of Mathematics, University of Birmingham, U.K.

Final Report for Grant award no. FA8655-08-1-3044
Government Program Manager: Dr. Gregg Abate
Total award period: 15 October 2008 to 14 October 2011

Contents

List of Figures	6
Summary	7
1 Introduction	8
2 Methods, Assumptions, and Procedures	10
2.1 Porous boundary	11
2.1.1 Regular microstructure	12
2.1.2 Mesh microstructure	12
2.1.3 Random microstructure	13
3 Linear stability problem	13
4 Neutral results	15
4.1 Regular microstructure	15
4.2 Mesh microstructure and random microstructure	16
5 Spatial Growth Rates	19
6 Maximum Spatial Growth Rates	20
7 Nonlinear analysis	23
7.1 The second-order problem	28
7.2 The third-order problem	28
8 Nonlinear results	29
8.1 Solid wall	30
8.2 Effect of the shock	34
8.3 Effect of porous walls	36
9 Discussion and conclusions	40
References	46
Appendix A	47
Appendix B	50

List of Figures

1	The geometry of the cone and shock. The cone is taken to be of semi-angle θ_c with the attached conical shock making an angle θ_s with the surface of the cone.	10
2	Neutral values of frequency Ω for the first four axisymmetric modes as a function of radius a with $n=0$ and $a/r_s = 0.57$: --- regular porous wall; — solid wall.	16
3	Neutral values of frequency Ω for the first five non-axisymmetric modes as a function of radius a with $a/r_s = 0.57$: --- regular porous wall; — solid wall; (a) $n = 1$, (b) $n = 2$	17
4	Neutral values of frequency Ω for the first four axisymmetric modes as a function of radius a with $n=0$ and $a/r_s = 0.57$: --- mesh microstructure; — random microstructure.	18
5	Neutral values of frequency Ω for the first five non-axisymmetric modes as a function of radius a with $n=1$ and $a/r_s = 0.57$: --- mesh microstructure; — random microstructure.	18
6	Spatial growth-rate parameters $\alpha_i(\Omega)$ for the first few non-neutral axisymmetric modes for $a/r_s = 0.57$: (a) $a = 0.6$; (b) $a = 1.0$; (c) $a = 1.5$; (d) $a = 2.0$: --- regular porous wall; — solid wall.	20
7	Spatial growth-rate parameters $\alpha_i(\Omega)$ for the first few non-neutral non-axisymmetric modes for $a/r_s = 0.57$ and $n = 1$: (a) $a = 0.6$; (b) $a = 1.0$; (c) $a = 1.5$; (d) $a = 2.0$: --- regular porous wall; — solid wall.	21
8	Spatial growth-rate parameters $\alpha_i(\Omega)$ for the first few non-neutral non-axisymmetric modes for $a/r_s = 0.57$ and $n = 2$: (a) $a = 0.6$; (b) $a = 1.0$; (c) $a = 1.5$; (d) $a = 2.0$: --- regular porous wall; — solid wall.	22
9	Spatial growth-rate parameters $\alpha_i(\Omega)$ for the first few non-neutral axisymmetric modes for $a/r_s = 0.57$: (a) $a = 0.6$; (b) $a = 1.0$; (c) $a = 1.5$; (d) $a = 2.0$: --- mesh microstructure; — random microstructure.	23
10	Spatial growth-rate parameters $\alpha_i(\Omega)$ for the first few non-neutral non-axisymmetric modes for $a/r_s = 0.57$ and $n = 1$: (a) $a = 0.6$; (b) $a = 1.0$; (c) $a = 1.5$; (d) $a = 2.0$: --- mesh microstructure; — random microstructure.	24
11	Neutral values of frequency Ω for the first five non-axisymmetric modes as a function of radius a for a regular microstructure with $n=1$ and $a/r_s = 0.57$: --- Kn=0.494; — Kn=0.	25
12	Spatial growth-rate parameters $\alpha_i(\Omega)$ for the first few non-neutral non-axisymmetric modes for a regular microstructure for $a/r_s = 0.57$, $n = 1$ and $a = 0.6$: --- Kn=0.494; — Kn=0.	25
13	Maximum spatial growth rates σ_{\max} for varying porosity ϕ_0 for a regular microstructure for $n = 1$, $a/r_s = 0.57$, $r_p^* = 30\mu m$ and $a = 0.8$	26

14	Maximum spatial growth rates σ_{\max} for varying pore radius r_p^* for a regular microstructure for $n = 1$, $a/r_s = 0.57$, $\phi_0 = 0.25$ and $a = 0.8$	26
15	Maximum spatial growth rates σ_{\max} for varying pore depth ratio h/r_p for a regular microstructure for $n = 1$, $a/r_s = 0.57$, $\phi_0 = 0.25$, $r_p^* = 30\mu m$ and $a = 0.8$	27
16	Maximum spatial growth rates σ_{\max} for varying pore depth h^* for $n = 1$, $a/r_s = 0.57$, $\phi_0 = 0.25$ and $a = 0.8$ for a mesh microstructure for $\tilde{a} = 0.05mm$	27
17	Maximum spatial growth rates σ_{\max} as a function of L^* for a regular microstructure for $n = 0, 1, 2, 3$, $a/r_s = 0.57$, $\phi_0 = 0.2$ and $r_p^* = 25\mu m$	28
18	(a) $\text{Re}(a_2/a_1)$; (b) $\text{Re}(a_3/a_1)$, as a function of local cone radius a for the first five modes. Results are shown for solid wall with $n = 1$ and $a/r_s = 0.57$	31
19	(a) $\text{Re}(a_2/a_1)$; (b) $\text{Re}(a_3/a_1)$, as a function of local cone radius a for the first five modes. Results are shown for a solid wall with $n = 2$ and $a/r_s = 0.57$	31
20	$\text{Re}(a_4/a_1)$ for the first five modes as a function of local cone radius a for (a) $0 \leq a \leq 1.0$; (b) $1.0 \leq a \leq 5.0$. Results are shown for a solid wall with $n = 1$ and $a/r_s = 0.57$	32
21	(a) $\text{Re}(a_4/a_1)$ for the first five modes as a function of local cone radius a for $0 \leq a \leq 2.3$. Results are shown for a solid wall with $n = 2$ and $a/r_s = 0.57$; (b) $\text{Re}(a_4/a_1)$ for the first mode as a function of a	33
22	$\text{Re}(a_4/a_1)$ for the first five modes as a function of local cone radius a for $2.3 \leq a \leq 5.0$. Results are shown for a solid wall with $n = 2$ and $a/r_s = 0.57$	33
23	(a) $\text{Re}(a_{20}/a_{10})$; (b) $\text{Re}(a_{40}/a_{10})$ for the first four modes as a function of local cone radius a . Results are shown for solid wall with $n = 0$ and $a/r_s = 0.57$. Results for the first mode are indicated by \circ	35
24	$\text{Re}(a_4/a_1)$ as a function of local cone radius a in the absence of shock. Results are shown for solid wall with (a) $n = 1$ and (b) $n = 2$	36
25	$\text{Re}(a_4/a_1)$ for the first five modes as a function of local cone radius a for $n = 1$ and $a/r_s = 0.57$: —, solid wall; — — —, regular microstructure model (6).	37
26	$\text{Re}(a_4/a_1)$ for the first five modes as a function of local cone radius a for $n = 2$ and $a/r_s = 0.57$: —, solid wall; — — —, regular microstructure model (6).	38
27	$\text{Re}(a_{40}/a_{10})$ for the first four modes as a function of local cone radius a for $n = 0$ and $a/r_s = 0.57$: —, solid wall; — — —, regular microstructure model (6). Results for the first mode are indicated by \bullet for solid wall and \circ for porous wall.	38
28	$\text{Re}(a_4/a_1)$ for the first five modes as a function of local cone radius a for $n = 1$ and $a/r_s = 0.57$: —, random microstructure model (11); — — —, regular microstructure model (6).	39
29	$\text{Re}(a_4/a_1)$ for the first five modes as a function of local cone radius a for $n = 1$ and $a/r_s = 0.57$: —, mesh microstructure model (8); — — —, regular microstructure model (6).	40

30	Re(a_4/a_1) as a function of local cone radius a for $a/r_s = 0.57$ and (a) $n = 0$; (b) $n = 1$. Results are shown using the regular microstructure model (6): —, $\phi_0 = \pi/4$; — — —, $\phi_0 = 0.2$. Symbols refer to mode number: \times , $m = 1$; \square , $m = 2$; \diamond , $m = 3$; \circ , $m = 4$; \bullet , $m = 5$	43
31	Re(a_4/a_1) as a function of local cone radius a for $a/r_s = 0.57$ and (a) $n = 2$; (b) $n = 3$. Results are shown using the regular microstructure model (6): —, $\phi_0 = \pi/4$; — — —, $\phi_0 = 0.2$. Symbols refer to mode number: \times , $m = 1$; \square , $m = 2$; \diamond , $m = 3$; \circ , $m = 4$; \bullet , $m = 5$	44
32	Re(a_3) for the first five modes as a function of spanwise wavenumber β_1 for $\bar{y}_s = 1.73$ (cf. equation 5.1 of Seddougui & Bassom 1994).	45

Summary

A theoretical linear stability analysis is used to consider the effect of a porous wall on the first mode of a hypersonic boundary layer on a sharp slender cone. The effect of curvature and of the attached shock are included for axisymmetric and non-axisymmetric disturbances. The flow in the hypersonic boundary layer is coupled to the flow in the porous layer. The linear results for neutral stability and spatial stability are presented for physical parameters and porous wall models, chosen to correspond to relevant experiments. The effects of varying the porous wall parameters are investigated. A weakly nonlinear stability analysis is carried out allowing an equation for the amplitude of disturbances to be derived. The coefficients of the terms in the amplitude equation are evaluated for axisymmetric and non-axisymmetric disturbances. The stabilising or destabilising effect of nonlinearity is found to depend on the cone radius. The presence of porous walls significantly influences the effect of nonlinearity.

1 Introduction

Transition to turbulence in hypersonic flows is associated with amplification of the first and/or second Mack modes. The first Mack mode is the high speed counterpart of Tollmien–Schlichting waves, so a viscous instability, with modes located close to the boundary. The second Mack mode is an inviscid instability. The second Mack mode is believed to be responsible for transition to turbulence on hypersonic slender bodies. Recent experiments by Fedorov *et al.* [1–3] have shown that a porous coating greatly stabilizes the second mode of the hypersonic boundary layer on sharp slender cones. The effect of the porous coating is to reduce the growth rates of the second mode to a level where they are comparable with those of the first mode (occurring at lower frequencies). In addition, the first mode is observed to be slightly destabilized by the presence of the porous coating. Thus, the first mode may now be more significant in the transition process.

Previous work [4] on the linear instability of the first modes (associated with Tollmien–Schlichting waves) in the hypersonic flow over a cone includes the effect of curvature and also the attached shock. The effect of curvature is significant with disturbances only existing over a finite range of wavenumbers for a fixed radius. Beyond a critical radius, dependent on the azimuthal wavenumber, all disturbances are damped. In [4] it was demonstrated that the effect of the shock, which allows incoming and outgoing waves, gives rise to multiple modes. It was demonstrated that the effect of the shock should not be neglected otherwise the correct effect of curvature will not be realized. The modes which exist in the absence of the shock are now totally destroyed. The effect of nonlinearity and curvature in hypersonic boundary layer flow has been considered in [5]. The current study investigates the effects of a porous layer on the first mode (viscous) for axisymmetric and non-axisymmetric disturbances. This is to confirm the experimental observations with a theory which includes the effect of curvature. The effect of curvature is of practical importance and has not been previously investigated theoretically for a porous coating. Also, if the second mode (and higher modes) are greatly stabilized then the first mode may well lead to transition to turbulence, particularly if the disturbances are triggered by wall roughness, since this mode is located close to the wall and governed by viscous effects.

We consider the effect of a porous wall on the linear instability and weakly nonlinear stability of hypersonic flow over a sharp slender cone. In this theoretical and asymptotic investigation for large Mach number and large Reynolds number the scales used will be appropriate to the first mode instability which is governed by a triple-deck structure. The effects of curvature and the attached shock will be taken into account. The effect of the porous wall will change the boundary condition on the normal velocity at the interface.

Our previous results have considered the effects of three different porous wall models used by other investigations; the porous wall model of Fedorov *et al.* [1] for a regular microstructure and a random microstructure [2] and a mesh microstructure used in the experiments of Lukashevich *et al.* [6]. The latter authors considered hypersonic flow over layers of stainless steel wire mesh. It was demonstrated experimentally and theoretically that a thinner layer of this structure is required to give optimal stabilisation of the second

Mack mode. Thus, it may be possible that this type of regular microstructure could be incorporated into thermal protection systems.

These porous wall cases are characterized by an admittance A_y which is a function of the disturbance frequency and depends on the physical properties of the flow and the porous layer. The focus of this report is the effect of these types of porous layers on the nonlinear stability of the first Mack mode.

In the first report the linear results were presented for axisymmetric disturbances. It was demonstrated that the effect of the porous wall was to reduce the neutral values slightly and gave rise to significantly larger growth rates than those for a solid wall for some parameter values. The second report considered linear stability for non-axisymmetric disturbances. It was shown that the destabilising effect of the porous wall was more significant for non-axisymmetric disturbances. The third report considered the effects of the porous wall properties on the maximum spatial growth rates obtained from the linear stability analysis. In particular, the effects of increasing pore radius, porosity and pore depth were shown to increase the spatial growth rates, although they did level off. The effects of gas rarefaction were also investigated. In addition, a nonlinear analysis was presented which lead to the derivation of an amplitude equation. The fourth report considered the linear stability of the hypersonic flow over a random microstructure using the theoretical model of Fedorov *et al.* [2] appropriate to a felt metal surface. It was found that the random microstructure has a larger destabilising effect than the regular microstructure, particularly for non-axisymmetric disturbances. Much larger growth rates were obtained for the random microstructure than for the regular microstructure. Thus, in a practical setting it is expected that a random microstructure may cause transition to turbulence if first modes are excited. These results agree with the numerical simulations of Wang and Zhong [7] who compared the effect of a felt-metal porous coating with that of a regular structure porous coating on Mack's first and second modes. The fifth report considered the flow over layers of fine mesh of square cross-section, motivated by the recent experiments of Lukashevich *et al.* [6]. The sixth report presented some results from the weakly nonlinear analysis for non-axisymmetric disturbances. These results showed that the nonlinear effects were destabilising.

This final report summarises all our findings. For simplicity, we consider flow relating to the previous experimental studies [1,2] and [6]. Thus, we concentrate on presenting linear and nonlinear results relating to physical situations.

In §2 the problem formulation is given for flow over the three types of microstructure previously investigated. In §3 the linear stability problem is summarised for axisymmetric and non-axisymmetric disturbances, resulting in two dispersion relations. §4 presents the results corresponding to experiments for neutrally stable disturbances, while §5 considers the effect of the porous walls on the spatial growth rates. In §6 the effect of varying the porosity, pore radius and pore depth are illustrated by considering the maximum spatial growth rates. Comparisons are also made for a porous surface optimised for second Mack mode stabilisation. In §7 the nonlinear analysis is outlined and the results are presented for axisymmetric and non-axisymmetric disturbances in §8. In §9 we draw some conclusions of our study.

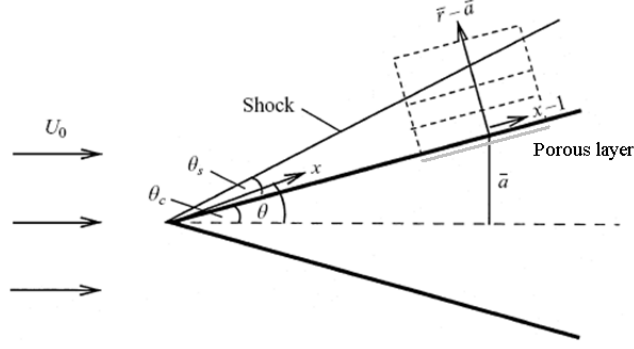


Figure 1: The geometry of the cone and shock. The cone is taken to be of semi-angle θ_c with the attached conical shock making an angle θ_s with the surface of the cone.

2 Methods, Assumptions, and Procedures

The flow of a compressible, viscous fluid over a sharp cone with a porous boundary, of semi-angle θ_c is considered at hypersonic speed U_0 aligned with its axis. We consider an attached conical shock which makes an angle θ_s with the cone; a situation which is illustrated in figure 1. Spherical polars (x, θ, ϕ) is the natural coordinate system in which to describe the basic flow, and here ϕ denotes the azimuthal angle. Furthermore, the radial distance x has been non-dimensionalised with respect to L^* , the distance from the tip of the cone to the location under consideration.

The approximate basic flow used is described in [4] so the complete details are omitted. The important features are summarised below. Away from the surface of the cone the flow satisfies the (inviscid) Euler equations. The velocities are non-dimensionalised with respect to U_- , where U_- is the magnitude of the fluid velocity just behind the shock. Additionally, the time, pressure and density are non-dimensionalised with respect to L^*/U_- , $\rho_- U_-^2$ and ρ_- respectively, where ρ_- is the density just behind the shock. Finally, the basic temperature is non-dimensionalised by T_- , the temperature just behind the shock.

The inviscid axisymmetric flow between the cone surface and the conical shock depends only on the polar angle θ . The jump conditions at the shock must be considered and the velocity components may be obtained from a numerical solution of the Taylor-Maccoll equation [8]. Since, for a hypersonic flow over a slender cone, the density does not vary much, we use the steady, constant-density solution given by [9], which has the advantage of analytical expressions for the velocity components and pressure. For a slender cone and hypersonic speeds these approximate solutions agree well with the exact (numerical) solutions.

From the hypersonic small-disturbance approximation to the basic flow given in [8], an approximate value of the shock angle may be obtained from the expression

$$\sin(\theta_s + \theta_c) = \sin \theta_c \left(\frac{\gamma + 1}{2} + \frac{1}{M_\infty^2 \sin^2 \theta_c} \right)^{1/2}, \quad (1)$$

where γ is the specific heat ratio and M_∞ denotes the Mach number in the free stream. For

the weak-shock solutions, relevant to the experiments, this gives excellent agreement with the exact solution. Note that the term $M_\infty \sin \theta_c$ is $O(1)$. Thus, the shock angle may be calculated, for a fixed cone angle and free-stream Mach number. A rough indication of the results is that $\theta_s \approx \theta_c$. This is consistent with our local analysis since we take the thickness of the upper deck (where the shock is located) to be comparable with the radius of the cone. Thus, the effect of the shock should not be neglected. The angle of the cone and the flow parameters enable the corresponding value of a to be obtained. Then, once the shock angle has been determined, the ratio a/r_s may be obtained simply from geometric arguments. We find for a slender cone that

$$\frac{a}{r_s} \approx \frac{\sin \theta_c}{\tan \theta_s + \sin \theta_c}, \quad (2)$$

where we have taken $\cos \theta_c \approx 1$. Since $\theta_s \approx \theta_c$ a rough approximation gives $a/r_s \approx 0.5$.

This solution is not valid close to the surface of the cone so a boundary-layer solution has to be introduced in this region. The Reynolds number of the flow is defined by $Re = \rho_- U_- L^* / \mu_-$. Taking the angle of the cone to be small the governing equations in the boundary-layer region are given in [4] in terms of dimensionless coordinates (x, \bar{r}, ϕ) and the Mach number, M , just behind the shock. Then $L^* \bar{r}$ is the normal direction to the cone surface, where $\bar{r} = \bar{a}$ on the generator of the cone. The corresponding non-dimensional velocities are (u, v, w) and the non-dimensionalised pressure and density p and ρ , respectively. The boundary conditions are no-slip at the surface of the cone (coupled to the porous layer) and appropriate conditions at the shock location. The non-dimensional temperature and viscosity at the surface of the cone are taken to be T_w and μ_w , respectively. The only restriction imposed on the temperature boundary condition is $T_w \gg 1$, which is violated only for situations involving strong cooling on the cone wall (see [4]). Usually the wall temperature is taken to be $T_w = T_b T_r$, where T_r is the adiabatic wall temperature given by $T_r = 1 + \sqrt{Pr} \frac{\gamma-1}{2} M^2$ where Pr is the Prandtl number. Thus, unless the constant T_b is very small, T_w will be of $O((\gamma-1)M^2)$ for both adiabatic walls ($T_b = 1$) or isothermal walls. The analysis is unaffected by the particular choice of temperature-viscosity law. The choice only affects the bounds placed on various parameters of the problem. Sutherland's viscosity law ($\mu_w \sim (1 + \bar{C}) T_w^{1/2}$, \bar{C} being a constant) is used henceforth.

2.1 Porous boundary

We will present results corresponding to porous surfaces used in the previous experimental investigations. In all cases the porous layer admittance A_y can then be expressed in the form

$$A_y = -(\phi_0/Z_0) \tanh(\Lambda h), \quad (3)$$

where ϕ_0 is the porosity. The porous layer parameters non-dimensionalised with respect to the boundary-layer displacement thickness δ^* so $h = h^*/\delta^*$ and $r_p = r_p^*/\delta^*$. Z_0 and Λ are the characteristic impedance and propagation constant of an isolated pore, respectively. Fedorov *et al.* [3] give the following expressions for the porous layer characteristics:

$$Z_0 = \frac{\sqrt{\rho_D/C_D}}{M\sqrt{T_w}} \quad \text{and} \quad \Lambda = \frac{i\omega M}{\sqrt{T_w}} \sqrt{\rho_D C_D}, \quad (4)$$

where ω is the disturbance frequency. These are functions of the complex dynamic density ρ_D and complex dynamic compressibility C_D . The precise definitions of these quantities depends on the structure of the porous wall and are given below for the cases investigated here.

The wall boundary condition, in all cases, is then given by

$$v = A_y (p - p_-), \quad (5)$$

where $p_- = \gamma^{-1} M^{-2}$.

2.1.1 Regular microstructure

Following [1] and [3] we consider the porous layer on the cone surface to be a sheet of thickness h^* perforated with cylindrical blind holes of radius r_p^* and equal spacing $s^* = r_p^* \sqrt{\pi/\phi_0}$. This model takes into account gas rarefaction effects. We have

$$\left. \begin{aligned} \rho_D &= \frac{1}{1 - F(B_\nu, \zeta)}, \quad C_D = 1 + (\gamma - 1)F(B_E, \zeta\sqrt{Pr}), \\ F(B_\nu, \zeta) &= \frac{G(\zeta)}{1 - 0.5B_\nu\zeta^2G(\zeta)}, \quad F(B_E, \zeta\sqrt{Pr}) = \frac{G(\zeta\sqrt{Pr})}{1 - 0.5B_E(\zeta\sqrt{Pr})^2G(\zeta\sqrt{Pr})}, \end{aligned} \right\} \quad (6)$$

where

$$B_\nu = (2\alpha_\nu^{-1} - 1)Kn, \quad B_E = [\gamma(2\alpha_E^{-1} - 1)/(\gamma + 1)Pr]Kn, \quad G(\zeta) = \frac{2J_1(\zeta)}{\zeta J_0(\zeta)}, \quad (7)$$

where $\zeta = r_p \sqrt{i\omega\rho_w R/\mu_w}$. Here $J_{0,1}$ are Bessel functions of the first kind, α_ν and α_E are molecular accommodation coefficients, Kn is the Knudsen number and R is the Reynolds number based on boundary-layer displacement thickness of the gas flow.

2.1.2 Mesh microstructure

Following [6] we consider the porous coating on the cone surface to comprise of several layers of stainless steel wire mesh as shown in figure 3 of their paper. A similar model to the one described in §2.1.1 for a regular microstructure is employed. Following Kozlov *et al.* [10] we have different expressions for the complex dynamic density and compressibility. Following [10] we can obtain the following expressions for the porous layer characteristics for a square mesh microstructure:

$$\left. \begin{aligned} \rho_D &= 1/(1 - F(\zeta)), \quad C_D = 1 + (\gamma - 1)F(\tilde{\zeta}), \\ F(\zeta) &= 1 + \zeta^2 \sum_{m=0}^{\infty} \left[\frac{2}{\gamma_m^2 \beta_m^2} \left(1 - \frac{\tanh(\beta_m)}{\beta_m} \right) \right], \\ F(\tilde{\zeta}) &= 1 + \tilde{\zeta}^2 \sum_{m=0}^{\infty} \left[\frac{2}{\gamma_m^2 \tilde{\beta}_m^2} \left(1 - \frac{\tanh(\tilde{\beta}_m)}{\tilde{\beta}_m} \right) \right], \end{aligned} \right\} \quad (8)$$

where

$$\gamma_m = \pi(m + \frac{1}{2}), \quad \beta_m = \sqrt{(\gamma_m^2 - \zeta^2)}, \quad \widetilde{\beta}_m = \sqrt{(\gamma_m^2 - \widetilde{\zeta}^2)}. \quad (9)$$

The characteristic size of an isolated pore is given by

$$\zeta = \sqrt{\frac{-i\omega\rho_w\widetilde{a}^2}{\mu_w}}R, \quad \text{and} \quad \widetilde{\zeta} = \sqrt{Pr}\zeta. \quad (10)$$

Here Pr is the Prandtl number taken as 0.72, \widetilde{a} is the pore width, R is the Reynolds number based on δ^* and γ is the ratio of specific heats of air. The flow parameters are chosen to fit the experimental conditions of [6].

2.1.3 Random microstructure

Following [2] we consider the porous layer on the cone surface to have a random microstructure. A similar model to the one used for the regular microstructure is employed. We have different expressions for the complex dynamic density and compressibility. Fedorov *et al.* [2] give the following expressions for the porous layer characteristics for flow over a felt-metal microstructure:

$$\left. \begin{aligned} \rho_D &= a_\infty \left(1 + \frac{g(\lambda_1)}{\lambda_1}\right), \quad C_D = \gamma - \frac{\gamma - 1}{1 + \frac{g(\lambda_2)}{\lambda_2}}, \\ g(\lambda) &= \sqrt{1 + \frac{4a_\infty\mu^*\lambda}{\sigma^*\phi_0r_p^{*2}}}, \quad \lambda_1 = \frac{ia_\infty\rho_w^*\omega^*}{\phi_0\sigma^*}, \quad \lambda_2 = 4Pr\lambda_1, \end{aligned} \right\} \quad (11)$$

where the characteristic pore size is

$$r_p^* = \frac{\pi d^*}{2(1 - \phi_0)(2 - \phi_0)}. \quad (12)$$

Here d^* is the fibre diameter. σ^* is the flow resistivity and its value is chosen to fit the experimental data for flow over the felt metal. The tortuosity a_∞ is taken to be unity. Following Fedorov *et al.* [2] rarefaction effects are neglected.

3 Linear stability problem

The linear stability of the basic flow described above for $M \gg 1$ and $Re \gg 1$ is investigated in the weak-interaction region following a triple-deck formulation used by [11] and [12]. The conditions to be satisfied at the shock by a disturbance to this basic flow must be specified and these have been derived in detail by [13]. The requisite constraints were obtained by considering the linearised jump conditions at the shock for infinitesimal waves beneath the shock; a similar procedure was adopted by [11] for flow over a wedge. Although the basic flow is not uniform in the regions below and above the shock, [13] showed that the jump conditions may still be evaluated at the undisturbed position of the shock. The condition satisfied by

the pressure amplitudes of the two acoustic waves (which are incident and reflected from the shock) is found to be similar to that for a wedge obtained by [11].

Attention is focused at a location on the surface of the cone with non-dimensional radius $\bar{a} = a^*/L^*$. It is assumed that $\bar{a}Re^{\frac{3}{8}}M^{\frac{1}{4}}\mu_w^{-\frac{3}{8}}T_w^{-\frac{9}{8}} = a \sim O(1)$ denotes the scale of the radius at this point; thus we have chosen $\sin\theta_c \sim \theta_c \sim Re^{-\frac{3}{8}}M^{-\frac{1}{4}}\mu_w^{\frac{3}{8}}T_w^{\frac{9}{8}}$. We note that in terms of the interaction parameter $\chi = M_\infty a^*/L^* \sim O(1)$ corresponding to a moderate inviscid interaction. Since from (1), $\theta_s \sim \theta_c$, the shock is located in the upper deck of the triple-deck structure.

Our study is confined to the question of the stability of the flow at a location on the body where the boundary-layer thickness is $O(Re^{-\frac{1}{2}}L^*)$, which is thin compared to the local radius of the cone. This situation is chosen so that curvature effects are significant. The analysis is somewhat simplified if non-parallel effects can be neglected and [11] showed that this is justifiable if the ‘Newtonian’ assumption $\gamma - 1 \ll 1$ is made. Thus, for simplicity, this condition is taken to hold in the following analysis although it can be easily relaxed for more involved studies.

It is convenient to scale out some of the parameters in the problem, namely μ_w , T_w and λ , where the last quantity denotes the boundary-layer skin friction. For axisymmetric flow the Mach number may be scaled out of the linear stability problem.

We consider perturbations proportional to

$$E = \exp [i(\alpha X + n\phi - \Omega\tau)],$$

where α and n are the streamwise and azimuthal wavenumbers respectively and Ω is the frequency of the disturbance. Note that n is an integer.

Previous scaling, following [11] and [14] is applied to the resulting equations for axisymmetric disturbances (corresponding to $n = 0$). Analytic solutions of these equations yields an eigenrelation relating the streamwise wavenumber α and frequency Ω , namely

$$\frac{\text{Ai}'(\xi_0)}{\int_{\xi_0}^{\infty} \text{Ai}(\xi)d\xi} = -(i\alpha)^{1/3} (\overline{A_Y} + i\alpha) \frac{I_0(i\alpha r_s)K_0(i\alpha a) - I_0(i\alpha a)K_0(i\alpha r_s)}{I_0(i\alpha r_s)K_1(i\alpha a) + I_1(i\alpha a)K_0(i\alpha r_s)}. \quad (13)$$

Here $\xi_0 = -i^{1/3}\Omega\alpha^{-2/3}$, $\text{Ai}(\xi)$ is the Airy function, $K_n(z)$ and $I_n(z)$ are the usual modified Bessel functions, and $A_y = Re^{-1/8}\mu_w^{1/8}\lambda^{1/4}T_w^{3/8}(M^2 - 1)^{3/8}\overline{A_Y}$. The admittance, A_y , is a function of the disturbance frequency and depends on the physical properties of the flow and the porous layer. The angular frequency of disturbance propagation through the pore is $\omega = (R/Re)Re^{1/4}\mu_w^{-1/4}\lambda^{3/2}T_w^{-3/4}(M^2 - 1)^{1/4}\Omega$, where R is the Reynolds number based on displacement thickness. The parameter r_s is the scaled non-dimensional location of the shock. The values of a and r_s depend on the physical parameters for the flow.

A similar analysis is applied for non-axisymmetric disturbances with azimuthal wavenumber n . The scaling is different and in particular $A_y = Re^{-1/8}\mu_w^{1/8}\lambda^{1/4}T_w^{3/8}M^{5/4}\overline{A_Y}$ and $\omega = (R/Re)Re^{1/4}\mu_w^{-1/4}\lambda^{3/2}T_w^{-3/4}M^{-1/2}\Omega$. The resulting eigenrelation for non-axisymmetric disturbances is given by

$$\frac{\text{Ai}'(\xi_0)}{\int_{\xi_0}^{\infty} \text{Ai}(\xi)d\xi} = (i\alpha)^{1/3} \left[\overline{A_Y} + \frac{in^2}{\alpha a^2} \right] \frac{I_n(i\alpha r_s)K_n(i\alpha a) - I_n(i\alpha a)K_n(i\alpha r_s)}{I_n(i\alpha r_s)K'_n(i\alpha a) - I'_n(i\alpha a)K_n(i\alpha r_s)}. \quad (14)$$

In order to present our results in regimes of practical interest, we will use the flow parameters from the relevant experimental studies [1,2] and [6]. The cone angle and Mach number from the experiments will determine the shock angle θ_s and the scaled radius a . Then the scaled shock location r_s is determined as described above. The experimental conditions correspond to $a/r_s = 0.57$ thus, we choose to present our results for this case.

The values for flow of a perfect gas were chosen as $M = 5.3$, $T_w = T_{ad}$, $\gamma = 1.4$, $Pr = 0.71$, $Re_1 = 15.2 \times 10^6$, $T_-^* = 56.4K$ and $\alpha_\nu = \alpha_E = 0.9$. These values correspond to the ones used in the previous numerical studies of [15]. The experiments were conducted on a cone of 0.5m in length.

4 Neutral results

We now consider neutrally stable solutions of the dispersion relations (13) and (14) corresponding to the axisymmetric case and the non-axisymmetric case, respectively. We seek solutions with α and Ω real and investigate the effect of the porous microstructure on the neutral solutions. The presence of the shock allows for multiple modes of solutions.

4.1 Regular microstructure

The current results for the regular microstructure comprising a regular array of cylindrical pores of circular cross-section are compared to the results for a solid wall for axisymmetric and non-axisymmetric modes.

For the regular microstructure of [3] the results presented below are for the porous layer parameters $r_p^* = 28.5\mu m$, $\phi_0 = 0.2$ and $h^* \gg r_p^*$. The last relation implies that $\Lambda h \rightarrow \infty$ so Eq. (3) simplifies to $A_y = -\phi_0/Z_0$. The effect of pore depth is investigated in section 6. The porous layer characteristics correspond to experimental values used in [3].

The flow conditions match the experimental conditions of [6]. Here a cone of angle $\theta_c = 7^\circ$ was used with a flow of Mach number $M_\infty = 6$.

The effects of rarefaction are included and the Knudsen number is calculated from the expression

$$Kn = \frac{\mu_w M}{r_p R} \sqrt{2\pi\gamma T_w},$$

giving $Kn = 0.494$.

Figure 2 shows the neutral values of frequency Ω as a function of radius a for the first four axisymmetric modes for $a/r_s = 0.57$. The scaled radius varies linearly with L^* . The range $0 < a < 5$ corresponds to $0 < L^* < 0.02m$ for axisymmetric modes for all the wall models considered. The dashed lines are for the porous wall and the solid lines correspond to the results for a solid wall from [4]. The flow is unstable in regions above these curves. For the higher modes for the solutions for α there is no discernible difference between the results (not shown). However, the neutral solutions for Ω are lower than those for a solid

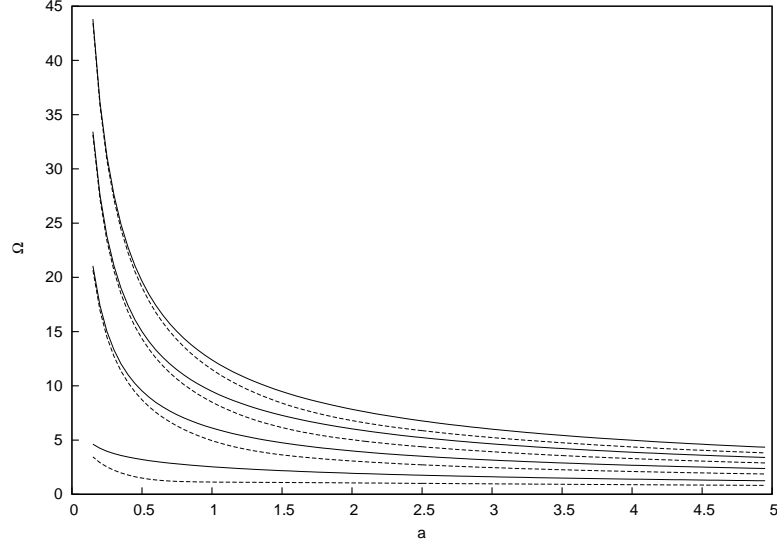


Figure 2: Neutral values of frequency Ω for the first four axisymmetric modes as a function of radius a with $n=0$ and $a/r_s = 0.57$: - - - regular porous wall; — solid wall.

wall, particularly for larger values of a . Thus, the flow over the porous surface will become unstable for lower frequencies than those for the solid wall.

Figure 3 shows the neutral solutions for Ω as a function of a for non-axisymmetric disturbances for $a/r_s = 0.57$ and $n = 1$ and $n = 2$ for a solid wall and a regular microstructure. For $n = 1$ the range $0 < a < 5$ corresponds to $0 < L^* < 14\text{m}$. Again the porous wall has only a small effect on the neutral values of α (not shown). The behaviour of the first mode is different from the higher modes with $\Omega \rightarrow 0$ as $a \rightarrow 0$. We see from figure 3 that the porous wall has a very small effect on the neutral values of Ω for this first mode. However, the porous wall has a significant effect on the higher modes, leading to lower neutral values of Ω . Thus, the effect of the porous wall is destabilising. Moreover, this effect increases for the higher modes. Similar results have been obtained for $n = 3$.

4.2 Mesh microstructure and random microstructure

The neutral results for the felt-metal microstructure are compared to those for a mesh microstructure. Following [6] we consider the mesh microstructure to correspond to $\phi_0 = 0.8$ and $\tilde{a} = 0.05\text{mm}$. In the experiments the porosity of the mesh microstructure is larger than that of the regular array of circular pores. This will lead to a larger destabilising effect on the first Mack mode (see section 5). We show our results for $h^* \gg \tilde{a}$.

Figure 4 shows the neutral values of Ω as a function of a for the mesh microstructure and the felt-metal microstructure for the first four axisymmetric modes. We find that the felt metal has a larger destabilising effect than the mesh microstructure, resulting in lower

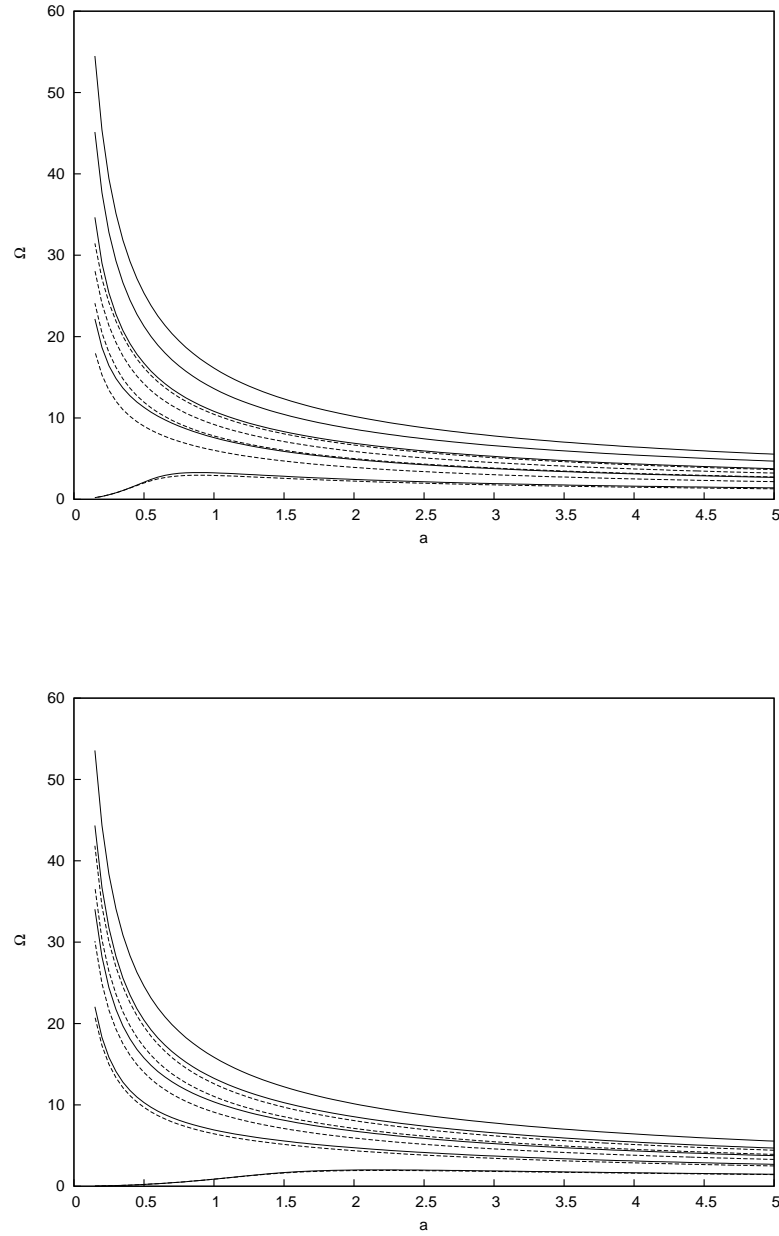


Figure 3: Neutral values of frequency Ω for the first five non-axisymmetric modes as a function of radius a with $a/r_s = 0.57$: --- regular porous wall; — solid wall; (a) $n = 1$, (b) $n = 2$.

values of neutral frequency.

Figure 5 shows the neutral solutions for Ω as a function of a for non-axisymmetric disturbances for $n = 1$ and $a/r_s = 0.57$ for a mesh microstructure and a random microstructure for the first five modes. The neutral values of Ω for the mesh microstructure are lower than

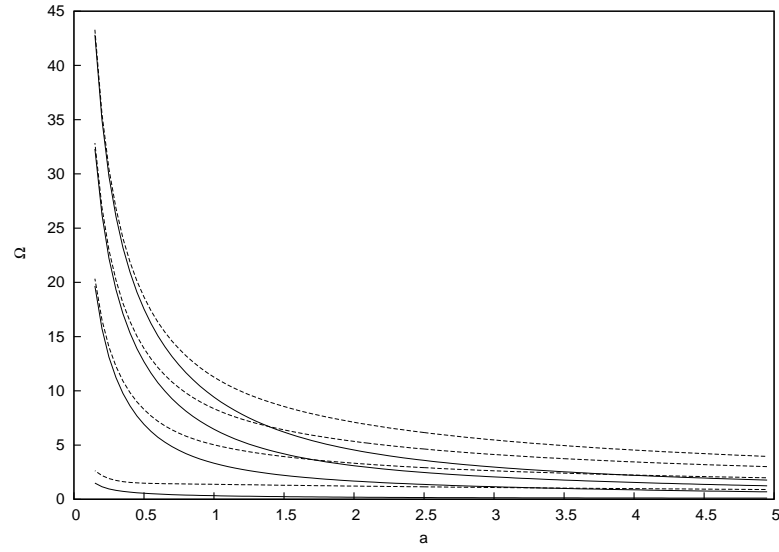


Figure 4: Neutral values of frequency Ω for the first four axisymmetric modes as a function of radius a with $n=0$ and $a/r_s = 0.57$: --- mesh microstructure; — random microstructure.

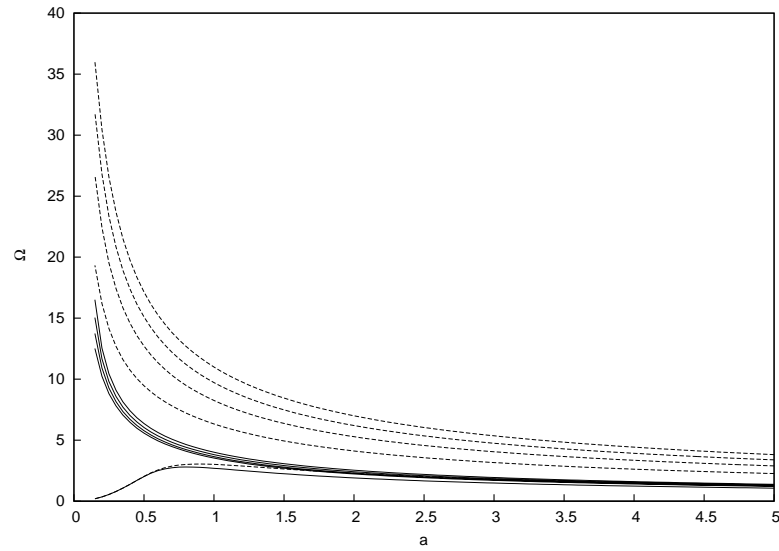


Figure 5: Neutral values of frequency Ω for the first five non-axisymmetric modes as a function of radius a with $n=1$ and $a/r_s = 0.57$: --- mesh microstructure; — random microstructure.

those for the regular microstructure comprising circular pores as a result of the porosity being larger. We see from figure 5 that the random microstructure has a significant destabilising effect, with the neutral values much lower than those for the mesh microstructure.

5 Spatial Growth Rates

We now concern ourselves with an examination of the spatial evolution of disturbances so that we concentrate on solutions of Eq. (13) and Eq. (14) with Ω real and α complex. If $\alpha = \alpha_r + i\alpha_i$ then $\alpha_i > 0$ is indicative of stability while $\alpha_i < 0$ denotes spatial instability.

Figures 6–8 show the dependence of the spatial growth-rate parameter α_i on the mode frequency Ω for a regular microstructure compared to a solid wall for $n = 0$, $n = 1$ and $n = 2$, respectively. The results are shown for $a/r_s = 0.57$ and $a = 0.6, 1.0, 1.5$ and 2.0 . There is a complete family of modes, as we saw in our account of neutral disturbances, and it is clear that for each member of the family there is a cut-off frequency Ω_c such that for $\Omega < \Omega_c$ that particular mode is stable but it becomes unstable if $\Omega > \Omega_c$. The effect of the neutral values being altered by the presence of the porous wall for all wall models leads to variation in the growth rates. The maximum values of $(-\alpha_i)$ for the porous wall are increased greatly from those of a solid wall for each mode.

In addition, we also observe that the growth rate for the porous modes does not rapidly approach zero at high frequencies, as is the case for the solid wall. Figure 6 shows that for the porous wall and the solid wall the first mode has the largest growth rate for axisymmetric disturbances for smaller values of a . However, for larger values of a the second mode has the largest maximum growth rate. As a increases the growth rates decrease.

From figure 7 we see that for non-axisymmetric modes with $n = 1$ the growth rate of the higher modes is greatly enhanced by the regular porous wall. It is the last mode shown which has the highest growth rate. The results for α_i presented in figure 8 for $n = 2$ are similar to those for $n = 1$.

Figure 9 shows the results for α_i for the felt-metal microstructure with $\phi_0 = 0.75$. These are compared to the values for a mesh microstructure with $\phi_0 = 0.8$. The results are presented for $n = 0$, $a/r_s = 0.57$ and $a = 0.6, 1.0, 1.5, 2.0$. We find that the growth rates of all modes are increased greatly for the felt-metal microstructure compared to the mesh microstructure. For the felt-metal microstructure the first mode has the largest growth rate, switching to the second mode as the radius a increases. This occurs at a larger value of a than for the mesh microstructure. These results agree with numerical results for a random microstructure from [7].

Figure 10 shows the spatial growth rates for $n = 1$ for the mesh microstructure and the felt-metal microstructure. The effect of the felt-metal microstructure is to give a very large increase in the maximum growth rates, approximately four times in magnitude, compared to the mesh microstructure.

We end this discussion on the effects of a porous wall on the spatial growth rates by considering the effects of rarefaction for a regular microstructure comprising an array of

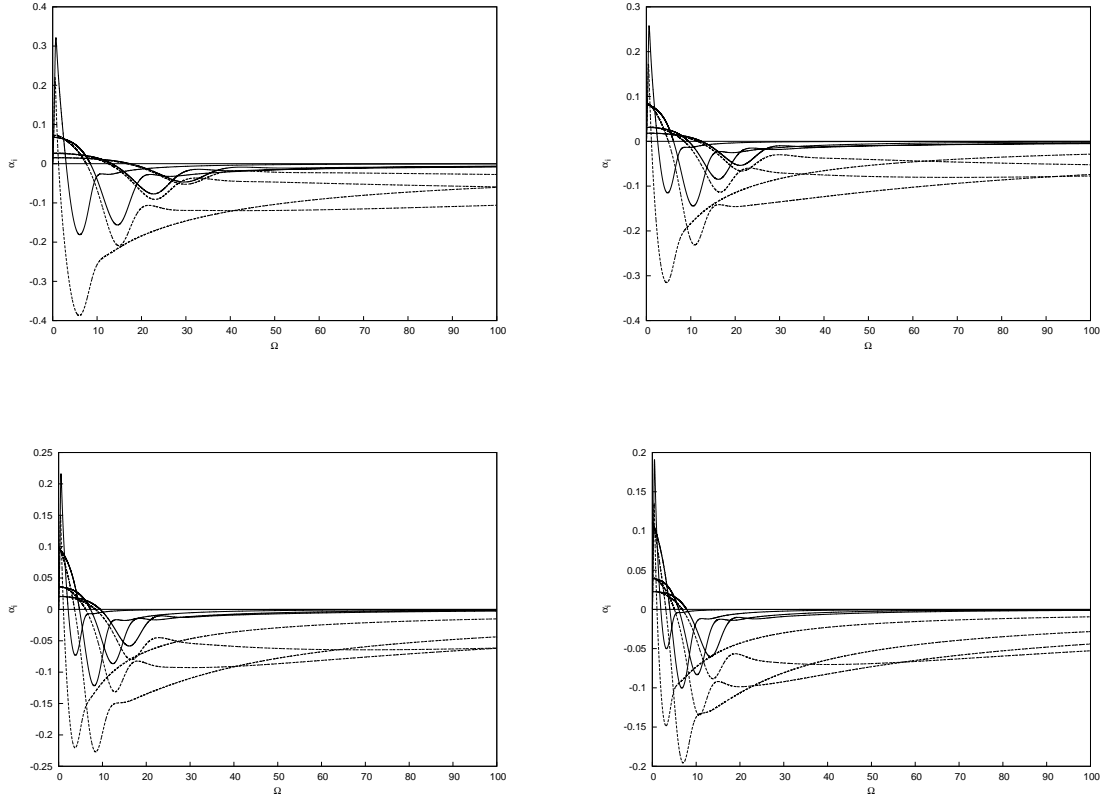


Figure 6: Spatial growth-rate parameters $\alpha_i(\Omega)$ for the first few non-neutral axisymmetric modes for $a/r_s = 0.57$: (a) $a = 0.6$; (b) $a = 1.0$; (c) $a = 1.5$; (d) $a = 2.0$: - - - regular porous wall; — solid wall.

circular pores. In figure 11 we show the neutral values of Ω as a function of a for the first five non-axisymmetric modes with $n = 1$, $a/r_s = 0.57$ for $Kn = 0$ and $Kn = 0.494$. We see that the effect of non-zero Knudson number is destabilising, with lower values of Ω compared to $Kn = 0$, particularly for the higher modes. The effect of rarefaction on the spatial growth rates is illustrated in figure 12, showing the results corresponding to figure 11. The growth rates are increased for non-zero Knudson number, with larger increases for the higher modes. We note that for the Mack second mode [8] found that the effect of rarefaction is stabilising.

6 Maximum Spatial Growth Rates

We investigate the effects of changing the properties of the porous wall on the linear stability of hypersonic flow over a sharp cone. We choose to concern ourselves with an examination of the effect of the physical properties of the porous layer on the maximum spatial evolution of disturbances. Thus, we consider the mode which has the largest value of $(-\alpha_i)$.

The effects of porosity, pore radius and pore depth on the maximum spatial growth rates

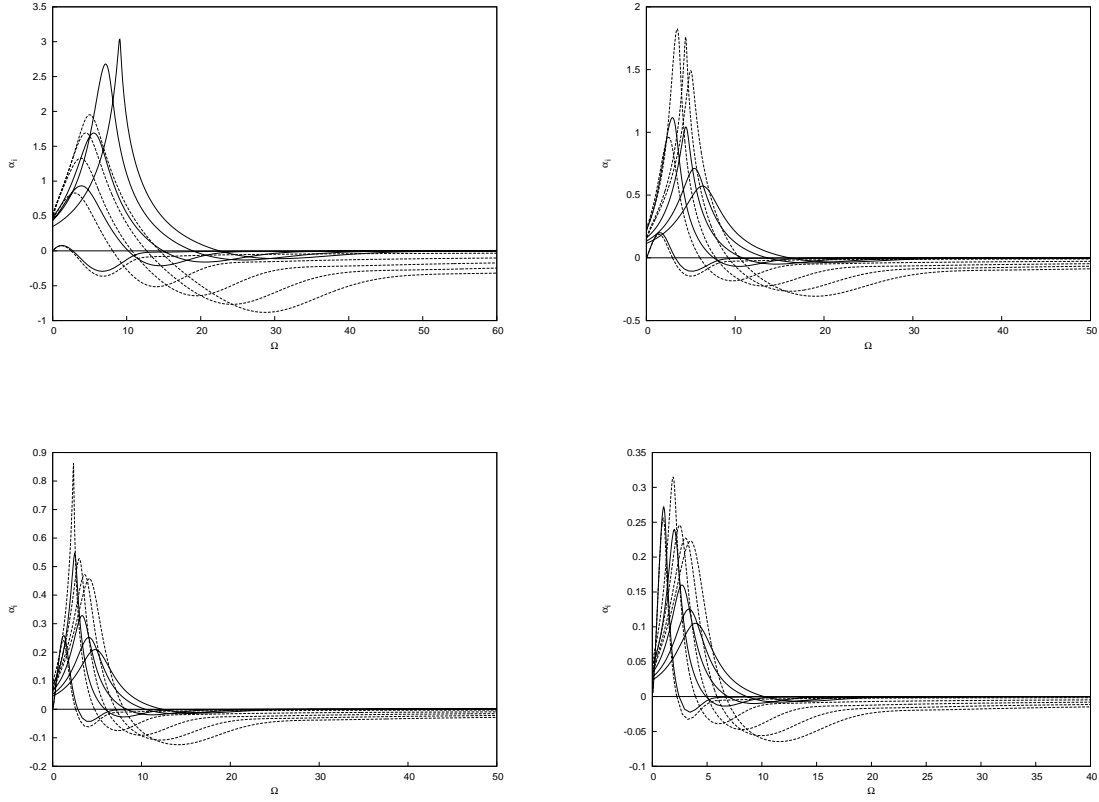


Figure 7: Spatial growth-rate parameters $\alpha_i(\Omega)$ for the first few non-neutral non-axisymmetric modes for $a/r_s = 0.57$ and $n = 1$: (a) $a = 0.6$; (b) $a = 1.0$; (c) $a = 1.5$; (d) $a = 2.0$: --- regular porous wall; — solid wall.

are considered for azimuthal wavenumber $n = 1$ and $a/r_s = 0.57$ and $a = 0.8$.

The effect of increasing the porosity ϕ_0 (by decreasing the pore spacing) for fixed pore radius $r_p^* = 30\mu m$ is illustrated in figure 13. We see that as the porosity increases the maximum spatial growth rate σ_{\max} increases. Here σ_{\max} is the maximum value of $-\alpha_i$ for the different modes for particular values of a/r_s .

In figure 14 we show the effect of the pore radius, r_p^* , on the maximum spatial growth rate σ_{\max} for $\phi_0 = 0.25$. We see that larger pore radius leads to larger maximum spatial growth rates.

The previous results presented have been obtained by assuming an infinite pore depth. The effect of finite pore depth is demonstrated in figure 15 for porosity $\phi_0 = 0.25$ and $r_p^* = 30\mu m$. We see that as h/r_p increases the maximum spatial growth rate increases but it levels off for $h/r_p > 20$. In the experiments the perforated sheet was relatively thick with $h^* = 0.45\text{--}0.5\text{mm}$ and $r_p^* = 25\text{--}30\mu m$, giving $h/r_p = 15\text{--}20$. This verifies our earlier assumption of taking $h/r_p \gg 1$ in our calculations. Previous calculations determined that maximum stabilisation of the second Mack mode was achieved for $h/r_p = 3$.

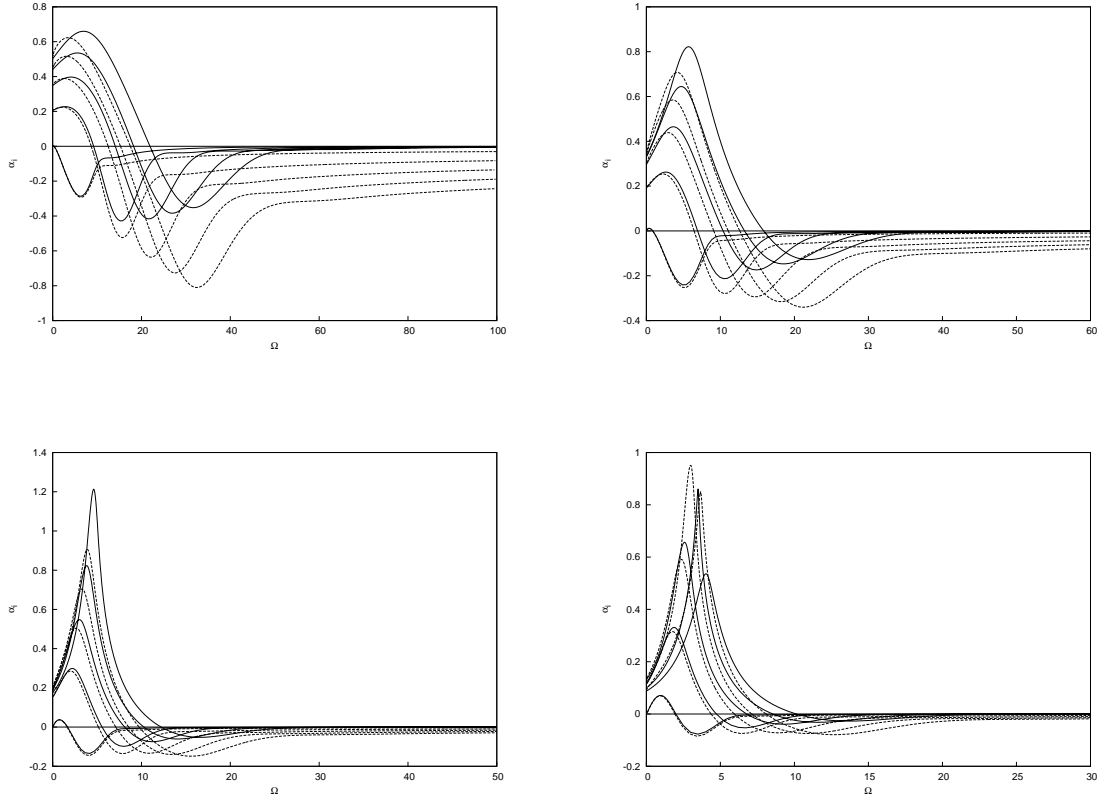


Figure 8: Spatial growth-rate parameters $\alpha_i(\Omega)$ for the first few non-neutral non-axisymmetric modes for $a/r_s = 0.57$ and $n = 2$: (a) $a = 0.6$; (b) $a = 1.0$; (c) $a = 1.5$; (d) $a = 2.0$: --- regular porous wall; — solid wall.

In figure 16 we show the effect of pore depth on a mesh microstructure. An increase in the depth corresponds to more layers of the fine mesh. We find that for $h^* = 0.15\text{mm}$ (corresponding to three layers of mesh) the maximum growth rate is a maximum for the first Mack mode. The previous results of [6] showed that $h^* = 0.15\text{mm}$ gave the maximum stabilisation of the second Mack mode. So this is the worst case for the first Mack mode.

In figure 17 we present the maximum spatial growth rates to correspond to the experimental conditions of Maslov [15] for a regular microstructure with $r_p^* = 25\mu\text{m}$, $\phi_0 = 0.2$ and $Re = 10 \times 10^6$. Here the dimensional spatial growth rate is shown as a function of the distance along the cone for the mode giving the largest growth rate for $n = 0, 1, 2, 3$ and $a/r_s = 0.57$. The dashed lines correspond to the porous wall and the solid lines correspond to a solid wall. We see that for the non-axisymmetric modes the growth rates are significantly larger for the porous wall compared to the solid wall. However, the size of the growth rates is much smaller than those obtained for the second Mack mode in [15].

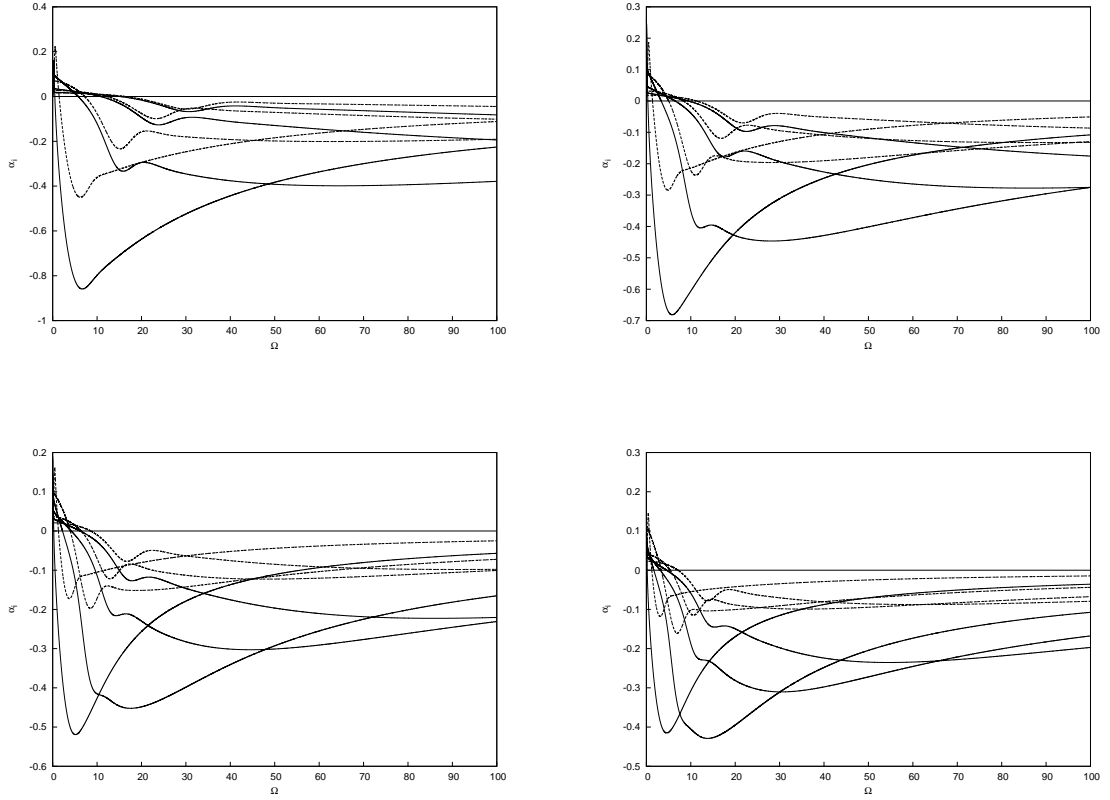


Figure 9: Spatial growth-rate parameters $\alpha_i(\Omega)$ for the first few non-neutral axisymmetric modes for $a/r_s = 0.57$: (a) $a = 0.6$; (b) $a = 1.0$; (c) $a = 1.5$; (d) $a = 2.0$: --- mesh microstructure; — random microstructure.

7 Nonlinear analysis

The linear stability analysis will not be valid for larger disturbances. Thus, it is important to determine the effect of nonlinearity on the stability of hypersonic boundary layer flow over a sharp slender cone with a porous wall. This has been investigated experimentally for second mode disturbances using the bicoherence method by Chokani *et al.* [16] and Bountin *et al.* [17]. We extend the linear analysis into the weakly nonlinear regime. Here larger disturbances are considered but not so large as to alter the basic flow. For the current problem with a solid wall this has been investigated by Stephen [5]. The planar case was considered previously by Seddougui and Bassom [18]. The lengthy analysis for the hypersonic flow over a cone with a porous closely follows these studies. Thus, the main results will be summarised and the differences highlighted.

We consider a weakly nonlinear disturbance which develops in the vicinity of a linear neutral point (real α and Ω for fixed $n > 0$). If the relative amplitude of the disturbance in the lower deck of the triple-deck structure is $O(h)$, $h \ll 1$, then the scaled amplitude A of

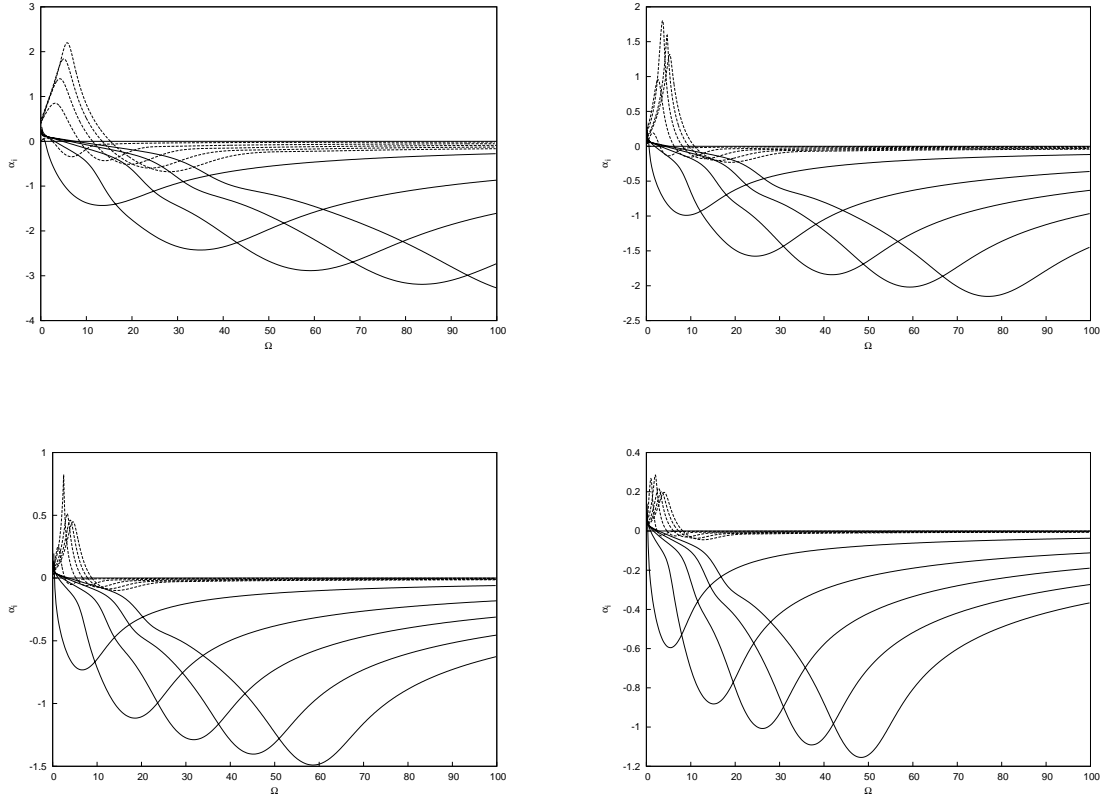


Figure 10: Spatial growth-rate parameters $\alpha_i(\Omega)$ for the first few non-neutral non-axisymmetric modes for $a/r_s = 0.57$ and $n = 1$: (a) $a = 0.6$; (b) $a = 1.0$; (c) $a = 1.5$; (d) $a = 2.0$: --- mesh microstructure; — random microstructure.

the mode will evolve on an $O(h^2)$ lengthscale. Thus, we consider perturbations at the point

$$x = 1 + h^2 x_2.$$

Since the skin friction λ is a function of x , it will also be slightly perturbed from its neutral value and we write

$$\lambda = 1 + h^2 \lambda_2,$$

where $\lambda_2 = x_2 d\lambda/dx|_{x=1}$. Additionally, we choose to fix the azimuthal wavenumber and write

$$\Omega = \Omega_1 + h^2 \Omega_2,$$

where Ω_1 is the neutral value of the frequency obtained from the linear stability problem. To account for the slow modulation of the amplitude on streamwise lengthscales we introduce the coordinate

$$\tilde{X} = h^2 X,$$

and then by use of multiple scales we replace all X derivatives throughout according to

$$\frac{\partial}{\partial X} \rightarrow \frac{\partial}{\partial X} + h^2 \frac{\partial}{\partial \tilde{X}}.$$

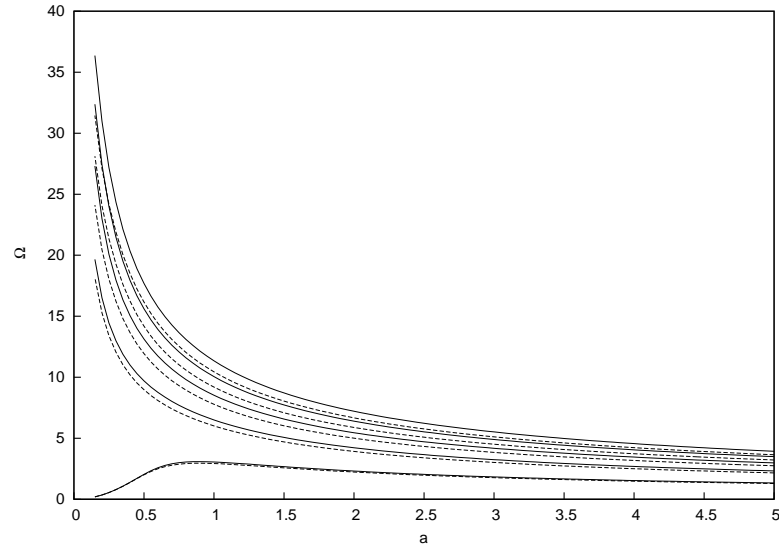


Figure 11: Neutral values of frequency Ω for the first five non-axisymmetric modes as a function of radius a for a regular microstructure with $n=1$ and $a/r_s = 0.57$: --- Kn=0.494; — Kn=0.

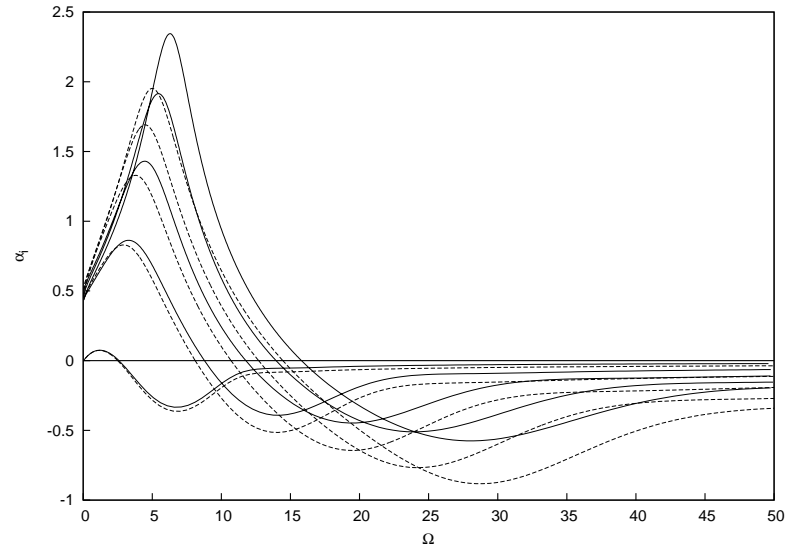


Figure 12: Spatial growth-rate parameters $\alpha_i(\Omega)$ for the first few non-neutral non-axisymmetric modes for a regular microstructure for $a/r_s = 0.57$, $n = 1$ and $a = 0.6$: --- Kn=0.494; — Kn=0.

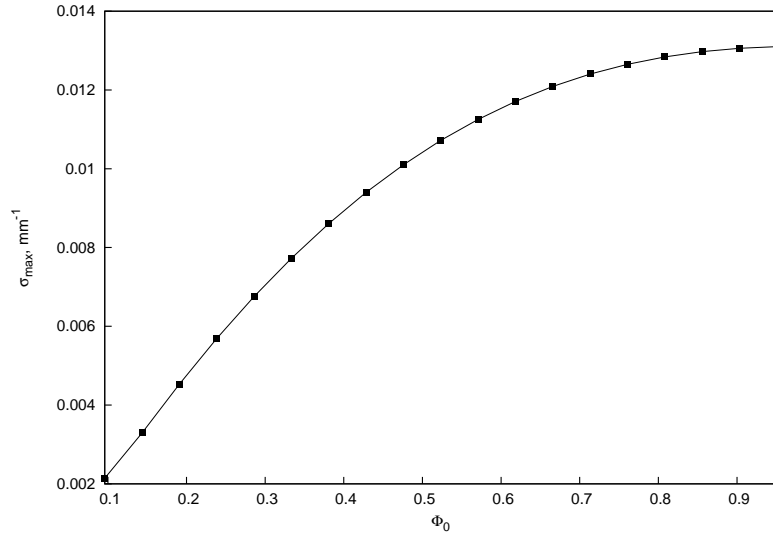


Figure 13: Maximum spatial growth rates σ_{\max} for varying porosity ϕ_0 for a regular microstructure for $n = 1$, $a/r_s = 0.57$, $r_p^* = 30\mu m$ and $a = 0.8$.

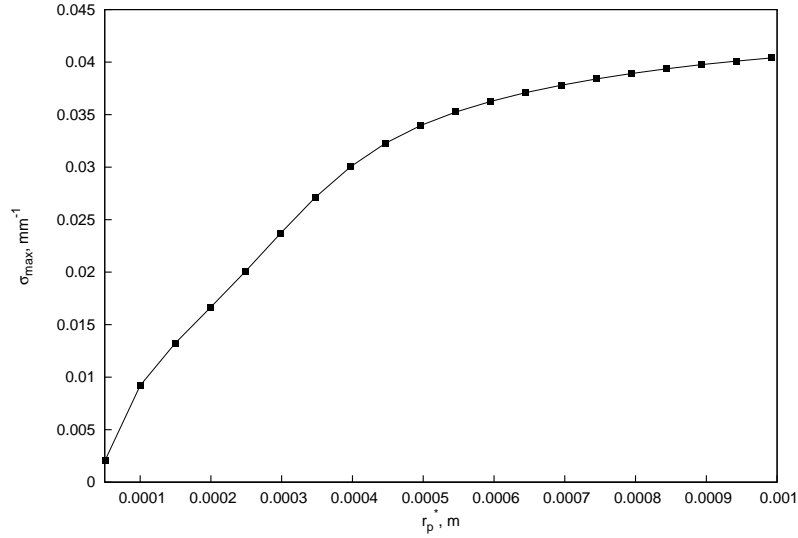


Figure 14: Maximum spatial growth rates σ_{\max} for varying pore radius r_p^* for a regular microstructure for $n = 1$, $a/r_s = 0.57$, $\phi_0 = 0.25$ and $a = 0.8$.

Now for $h \ll 1$ we proceed to seek solutions of the lower-deck equations ((8) and (9) in the

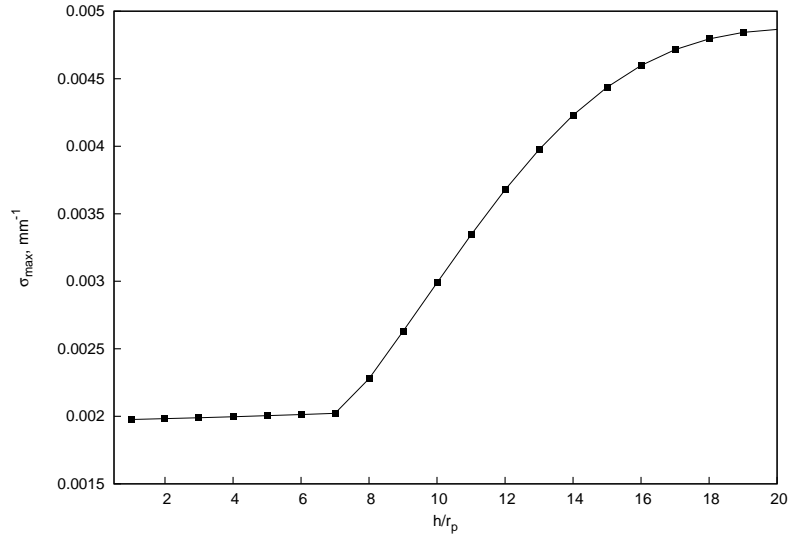


Figure 15: Maximum spatial growth rates σ_{\max} for varying pore depth ratio h/r_p for a regular microstructure for $n = 1$, $a/r_s = 0.57$, $\phi_0 = 0.25$, $r_p^* = 30\mu\text{m}$ and $a = 0.8$.

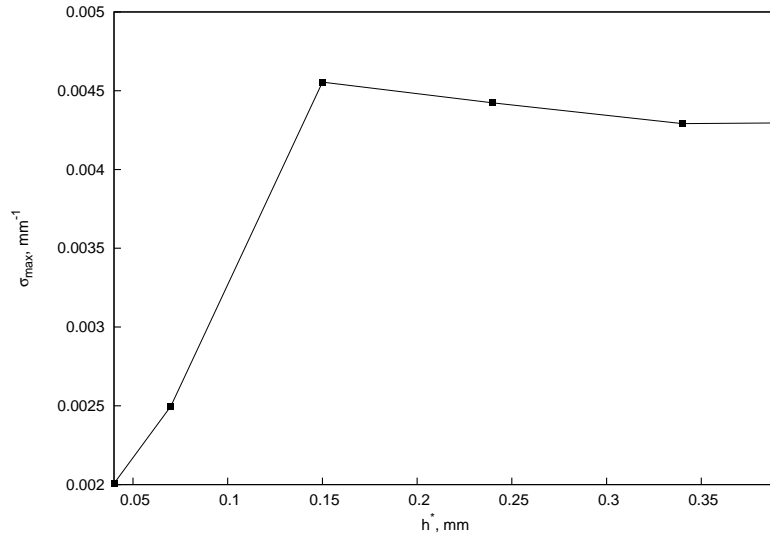


Figure 16: Maximum spatial growth rates σ_{\max} for varying pore depth h^* for $n = 1$, $a/r_s = 0.57$, $\phi_0 = 0.25$ and $a = 0.8$ for a mesh microstructure for $\tilde{a} = 0.05\text{mm}$.

second report) and the upper-deck problem ((11) in the second report) where

$$(U - (1 + h^2 \lambda_2) Y, V, W, P, A, \tilde{p}) = \sum_{j=1}^3 h^j (U_j, V_j, W_j, P_j, A_j, \tilde{p}_j) + O(h^4). \quad (15)$$

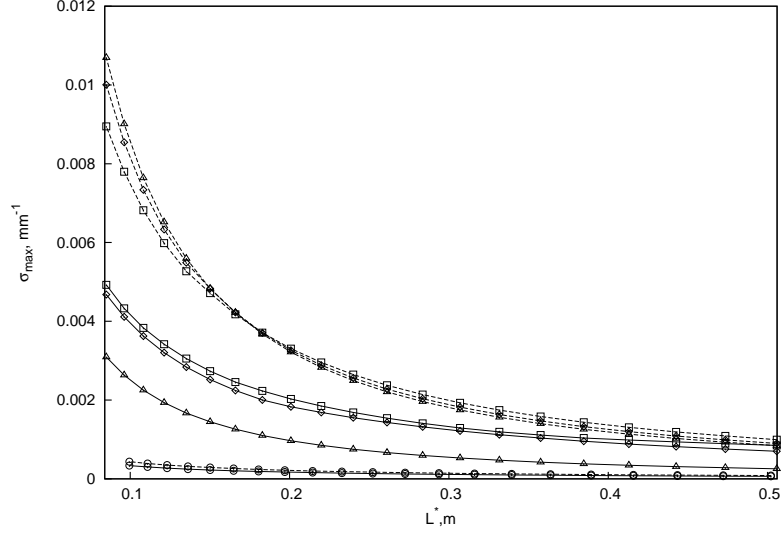


Figure 17: Maximum spatial growth rates σ_{\max} as a function of L^* for a regular microstructure for $n = 0, 1, 2, 3$, $a/r_s = 0.57$, $\phi_0 = 0.2$ and $r_p^* = 25\mu m$.

Substitution of (15) into the disturbance equations leads to a hierarchy of problems at increasing orders in h .

The solution for the $O(h)$ terms in (15) has been obtained from the linear stability analysis resulting in the dispersion relations (13) and (14). The solution for A_1 has the form

$$A_1 = A_{11}E + A_{11}^{(c)}E^{-1},$$

where the superscript (c) denotes complex conjugate.

7.1 The second-order problem

At $O(h^2)$ we find the solution for A_2 takes the form

$$A_2 = A_{22}E^2 + A_{20} + A_{22}^{(c)}E^{-2},$$

with similar expansions for U_2 , V_2 , W_2 , P_2 and \tilde{p}_2 . The analysis follows that for the solid wall problem (see Smith [19]) but the boundary condition at the porous wall leads to additional terms in the solutions. Solving the equations and satisfying all the boundary conditions leads to an expression relating the amplitude at $O(h^2)$ to the square of the amplitude at $O(h)$.

7.2 The third-order problem

At this order the amplitude equation for the unknown function $A_{11}(\tilde{X})$ is determined. This equation arises from a solvability condition on the $O(h^3E)$ terms. We seek solutions of the

form

$$\tilde{p}_3 = \tilde{p}_{31}E + \tilde{p}_{32}E^2 + \tilde{p}_{33}E^3 + \tilde{p}_{31}^{(c)}E^{-1} + \tilde{p}_{32}^{(c)}E^{-2} + \tilde{p}_{33}^{(c)}E^{-3} + \tilde{p}_{30}.$$

The solution in the lower deck involves an inhomogeneous differential equation of which a solution only exists if a certain compatibility condition holds. This condition is derived by considering the adjoint system of the problem as in Hall and Smith [20]. Specifically, we multiply the inhomogeneous equation by the adjoint function and integrate over the range $[\xi_0, \infty]$.

By matching the solution for \tilde{p}_{31} with the solution for the disturbance pressure in the main deck we obtain the evolution equation for A_{11} in the form

$$a_1 \frac{dA_{11}}{d\tilde{X}} = (a_2\lambda_2 + a_3\Omega_2) A_{11} + a_4 A_{11} |A_{11}|^2. \quad (16)$$

The complex constants in (16) are given by

$$\begin{aligned} a_1 = & -i^{4/3} \frac{T1}{\kappa} - \frac{n^2}{\alpha a^2} \frac{\text{Ai}'(\xi_0)}{\kappa} \mathbb{P}_1 \int_{\xi_0}^{\infty} [K(\xi)L(\xi)] d\xi - 2(i\alpha)^{1/3} \text{Ai}(\xi_0) \alpha \mathbb{P}_1^{-1} \\ & \times \left[(b_n f_n + c_n d_n) \left\{ K_n(i\alpha a) - \frac{\text{Ai}'(\xi_0)}{\kappa} (i\alpha)^{-1/3} \mathbb{P}_1 K'_n(i\alpha a) \right\} \right. \\ & \left. - (b_n d_n + c_n e_n) \left\{ I_n(i\alpha a) - \frac{\text{Ai}'(\xi_0)}{\kappa} (i\alpha)^{-1/3} \mathbb{P}_1 I'_n(i\alpha a) \right\} \right], \end{aligned} \quad (17)$$

$$a_2 = i^{-2/3} \alpha L2 + \alpha \kappa^{-1} \overline{A_Y} i^{1/3} T3, \quad (18)$$

$$a_3 = (i\alpha)^{1/3} \kappa^{-1} T18, \quad (19)$$

$$a_4 = \frac{i^{-2/3} (\alpha)^{5/3}}{\kappa |\kappa|^2} \left[L11 - \overline{A_Y} [\alpha^{2/3} \mathbb{P}_1 T22 - \mathbb{P}_2 T25 L12] - \overline{A_Y}^{(c)} \mathbb{P}_1^{(c)} L13 \right], \quad (20)$$

where $\kappa = \int_{\xi_0}^{\infty} \text{Ai}(s) ds$, $\mathbb{P}_1 = (\overline{A_Y} + \frac{in^2}{\alpha a^2})^{-1}$, $\mathbb{P}_2 = (\overline{A_Y} + 2\frac{in^2}{\alpha a^2})^{-1}$. All other abbreviations Tij , Lij are defined in Appendix A. The coefficients b_n , c_n , d_n , e_n , f_n depend on the neutral values of α for fixed values of a and r_s and involve modified Bessel functions. They are defined in the appendix of Stephen [5]. The remaining complex constants involve Airy functions and are defined in Appendix A. The coefficients are functions of the neutral results and so depend on the porous wall properties. The porous wall has introduced additional terms in the coefficients. Thus, their evaluation requires substantial numerical calculations.

The corresponding nonlinear problem for axisymmetric disturbances must be considered separately since the Mach number can be scaled out of the weakly nonlinear problem. The analysis is very similar to that for the non-axisymmetric problem and the resulting amplitude equation is presented in Appendix B.

8 Nonlinear results

We will begin this section by presenting the results of the nonlinear stability analysis for the solid wall with flow parameters corresponding to the experiments of [15] and [3]. This

was not done in [5]. We will then present corresponding results obtained using the different porous wall models and deduce the effect of the porous walls on the nonlinear stability.

8.1 Solid wall

In order to present our results in regimes of practical interest, we will use the flow parameters from the relevant experimental studies. Thus all our results are presented for $a/r_s = 0.57$.

We turn to the non-axisymmetric problem and the evolution equation (16). We can solve this equation using separation of variables. Following [21] we can determine an explicit expression for the amplitude $|A_{11}|^2$ as

$$|A_{11}|^2 = \frac{2\mathcal{K}e^{\mathcal{K}\tilde{X}}}{\left[\mathcal{K}C_1 - 2\text{Re}\left(\frac{a_4}{a_1}\right)e^{\mathcal{K}\tilde{X}}\right]},$$

where $\mathcal{K} = 2\text{Re}\left(\frac{a_2}{a_1}\lambda_2 + \frac{a_3}{a_1}\Omega_2\right)$ and C_1 is a constant of integration. When $\mathcal{K} > 0$ we have linear instability. Note that λ_2 is negative downstream of the neutral location. If then $\text{Re}\left(\frac{a_4}{a_1}\right) < 0$, nonlinear effects are stabilising and the linearly unstable mode is supercritically stable with an equilibrium amplitude given by

$$|A_{11}| = \sqrt{\frac{\text{Re}\left(\frac{a_2}{a_1}\lambda_2 + \frac{a_3}{a_1}\Omega_2\right)}{-\text{Re}\left(\frac{a_4}{a_1}\right)}}.$$

In figure 18a we show $\text{Re}(a_2/a_1)$ as a function of a for $n = 1$ corresponding to the first five neutral modes of (14) for a solid wall. The arrows here and on all the subsequent figures indicate increasing mode number. We can see that this quantity is always negative. The results for $n = 2$ are shown in figure 19a. The magnitudes are decreased when compared to $n = 1$. The corresponding values of $\text{Re}(a_3/a_1)$ are shown in figures 18b and 19b, respectively for $n = 1$ and $n = 2$. There is a difference in behaviour of $\text{Re}(a_3/a_1)$ for the first mode for small values of a , corresponding to the anomalous behaviour of the lowest neutral solution; see figure 3. The effect of increasing the azimuthal wavenumber is to increase the magnitude of $\text{Re}(a_3/a_1)$.

We now investigate the effect of nonlinearity on linearly unstable disturbances by considering the sign of $\text{Re}(a_4/a_1)$. In order to see the behaviour of the different modes the value of $\text{Re}(a_4/a_1)$ versus a for $0 \leq a \leq 1$ is shown in figure 20a and versus a for $1 \leq a \leq 5$ is shown in figure 20b for $n = 1$. In figures 20a and 20b we can see that the sign of $\text{Re}(a_4/a_1)$ is always positive for the first mode ($m = 1$). Thus nonlinear effects always destabilise this mode possibly leading to a subcritical instability. The effect of nonlinearity on the remaining four modes depends on the value of a . For $a < 1$, $\text{Re}(a_4/a_1) < 0$ leading to supercritical instability. As the value of a increases, the sign of $\text{Re}(a_4/a_1)$ becomes positive beginning with the higher modes indicating that nonlinear effects now destabilise these linearly unstable modes. In the limit of large a we can see that $\text{Re}(a_4/a_1) \rightarrow 0$ for all the modes, with the first mode

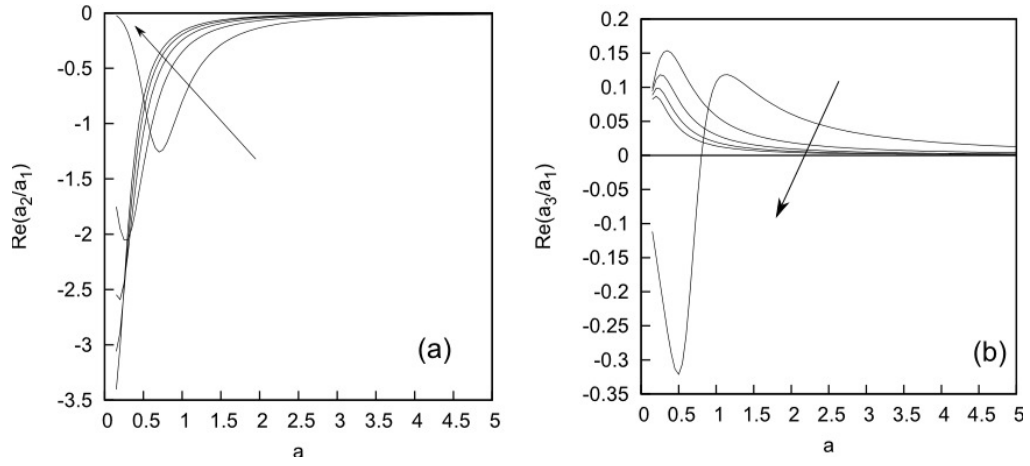


Figure 18: (a) $\text{Re}(a_2/a_1)$; (b) $\text{Re}(a_3/a_1)$, as a function of local cone radius a for the first five modes. Results are shown for solid wall with $n = 1$ and $a/r_s = 0.57$.

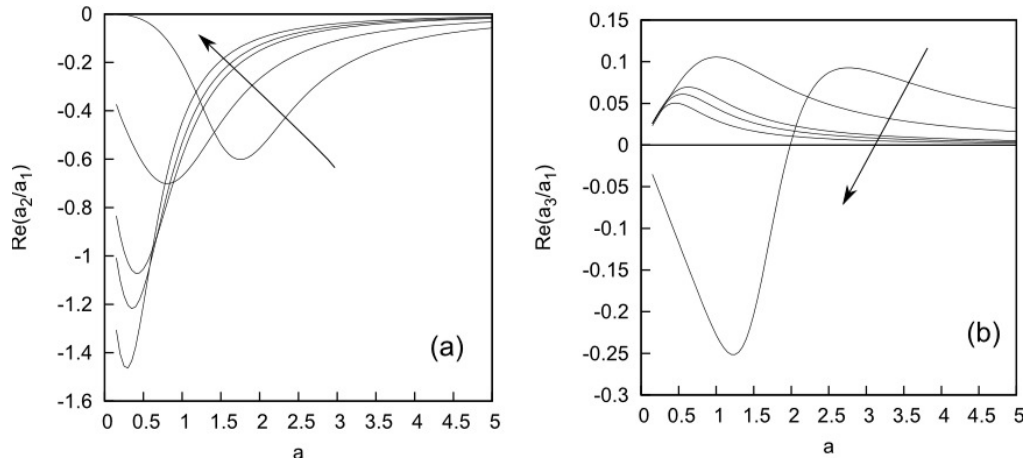
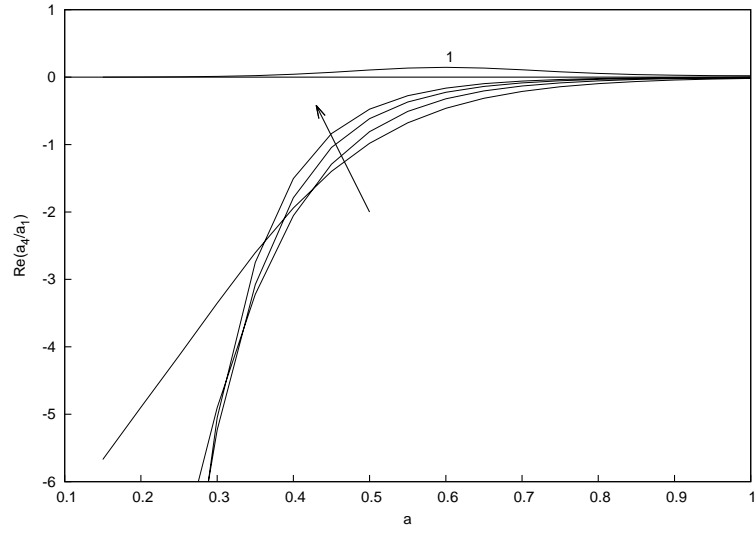
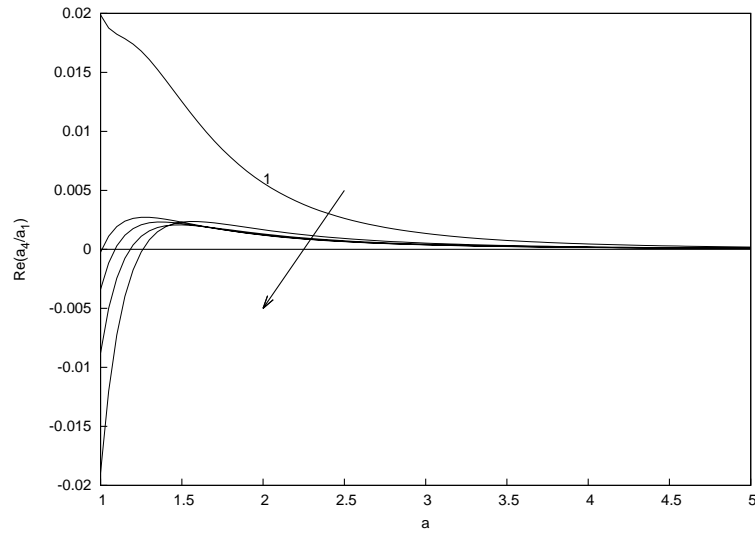


Figure 19: (a) $\text{Re}(a_2/a_1)$; (b) $\text{Re}(a_3/a_1)$, as a function of local cone radius a for the first five modes. Results are shown for a solid wall with $n = 2$ and $a/r_s = 0.57$.



(a)



(b)

Figure 20: $\text{Re}(a_4/a_1)$ for the first five modes as a function of local cone radius a for (a) $0 \leq a \leq 1.0$; (b) $1.0 \leq a \leq 5.0$. Results are shown for a solid wall with $n = 1$ and $a/r_s = 0.57$.

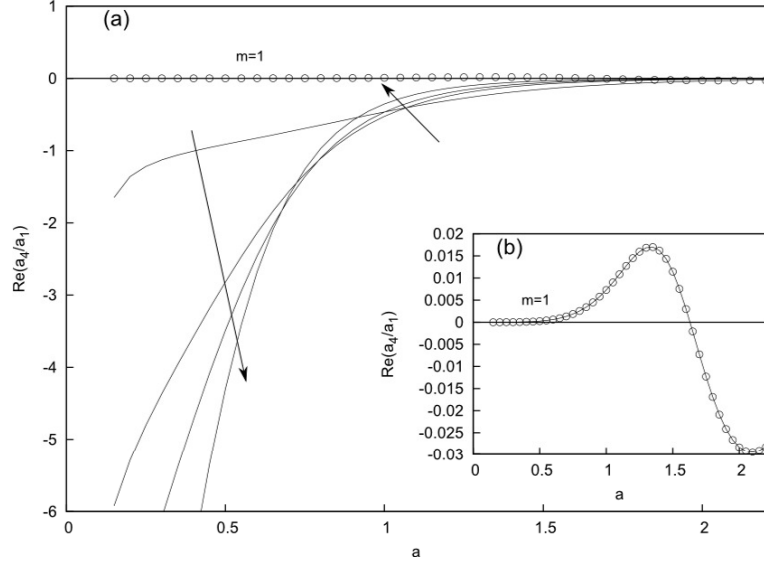


Figure 21: (a) $\text{Re}(a_4/a_1)$ for the first five modes as a function of local cone radius a for $0 \leq a \leq 2.3$. Results are shown for a solid wall with $n = 2$ and $a/r_s = 0.57$; (b) $\text{Re}(a_4/a_1)$ for the first mode as a function of a .

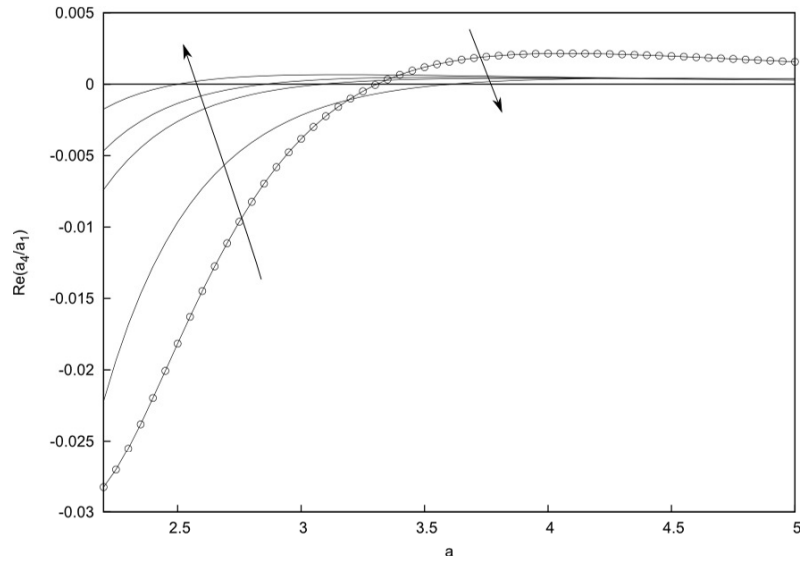


Figure 22: $\text{Re}(a_4/a_1)$ for the first five modes as a function of local cone radius a for $2.3 \leq a \leq 5.0$. Results are shown for a solid wall with $n = 2$ and $a/r_s = 0.57$.

having the highest amplitude. For a fixed cone angle the effect of increasing a is to move further along the cone surface. Thus at large streamwise distances we can expect nonlinear disturbance amplitudes to be very small. The corresponding results for $\text{Re}(a_4/a_1)$ with $n = 2$ can be seen in figures 21 and 22. In figure 21a we can see that effect of nonlinearity on mode numbers > 1 for $n = 2$ are similar to that for $n = 1$. Higher azimuthal wavenumber allows the stabilising effect of nonlinearity to persist for larger ranges of a . In figure 22 we see that $\text{Re}(a_4/a_1)$ becomes positive for $a > 2.3$ with the higher modes becoming destabilised first. The effect of azimuthal wavenumber is more significant on the first mode as can be seen in figure 21b. Here we see that the first mode is stabilised by nonlinearity for a narrow range of a ($\text{Re}(a_4/a_1) < 0$ when $1.6 < a < 3.3$). In the limit of large a nonlinear effects on the first mode persist while the effects on the higher modes diminish as $\text{Re}(a_4/a_1) \rightarrow 0$ for these modes. The effect of nonlinearity for disturbances with $n = 3$ have also been investigated. The results (not shown) indicate that overall trends remain similar to that for $n = 2$. We may thus conclude that nonlinear effects tend to stabilise the higher modes for a wider range of a for higher azimuthal wavenumbers, and the first mode becomes the most destabilised by nonlinearity at large values of a .

We consider the effect of nonlinearity on axisymmetric disturbances next. The neutral linear stability results for these disturbances were shown in figure 2. Axisymmetric disturbances are linearly unstable if $\text{Re}(a_{20}\lambda_2/a_{10}) > 0$. If $\text{Re}(a_{40}/a_{10}) < 0$ for these disturbances then nonlinear effects are stabilising and the linearly unstable modes are supercritically stable with an equilibrium amplitude

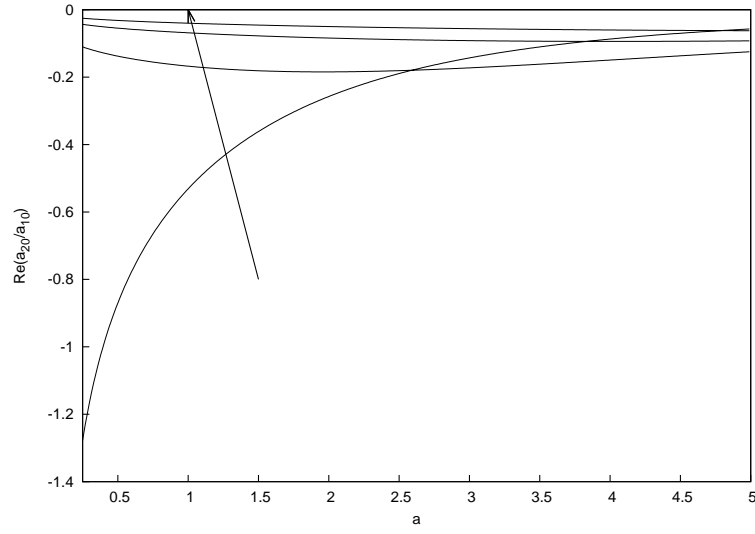
$$|A_{11}| = (-\lambda_2)^{1/2} \left(\frac{-\text{Re}(a_{20})}{-\text{Re}(a_{40})} \right)^{1/2}.$$

In figure 23a we can see $\text{Re}(a_{20}/a_{10})$ as a function of a . We notice that this quantity is always negative. Figure 23b shows $\text{Re}(a_{40}/a_{10})$ versus a corresponding to the first four modes. We see that this quantity is negative for all the modes with the exception of the first mode. For this mode $\text{Re}(a_{40}/a_{10})$ becomes slightly positive for $a > 2.3$. Thus, we can expect nonlinear effects to stabilise linearly unstable axisymmetric disturbances with the exception of the first mode which is slightly destabilised above a certain value of a .

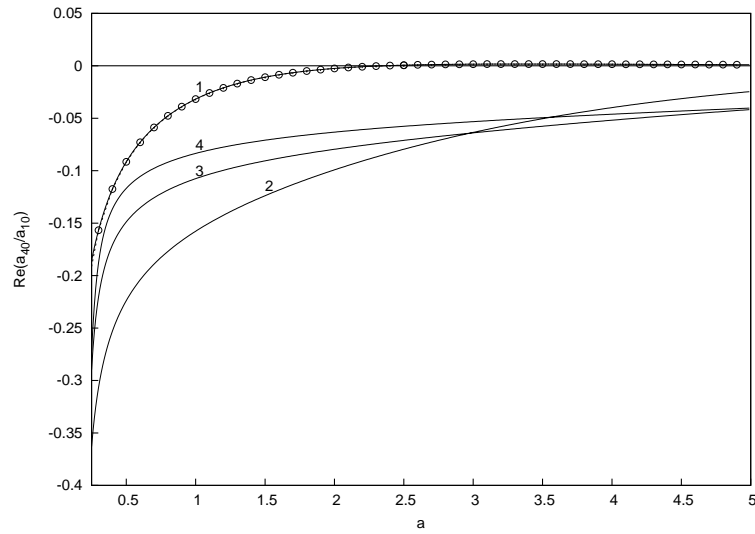
The results discussed above for $\text{Re}(a_{40}/a_{10})$ and $\text{Re}(a_4/a_1)$ differ from those presented in [5]. In that paper it was reported that $\text{Re}(a_{40}/a_{10})$ and $\text{Re}(a_4/a_1)$ were always negative, so the nonlinear effects were always stabilising. Our corrected results have shown the significant result that the nonlinear effects are destabilising for particular ranges of a . Moreover these ranges correspond to realistic values of the location of porous surfaces in experiments.

8.2 Effect of the shock

Before proceeding to investigate the effect of porous walls on the nonlinear stability it is useful to consider the stability problem in the absence of shock. The problem in the absence of a shock was first considered in [12] and [14]. It can be shown that the neutral curves in the absence of shock differ fundamentally from those in the presence of shock as solutions are



(a)



(b)

Figure 23: (a) $\text{Re}(a_{20}/a_{10})$; (b) $\text{Re}(a_{40}/a_{10})$ for the first four modes as a function of local cone radius a . Results are shown for solid wall with $n = 0$ and $a/r_s = 0.57$. Results for the first mode are indicated by \circ .

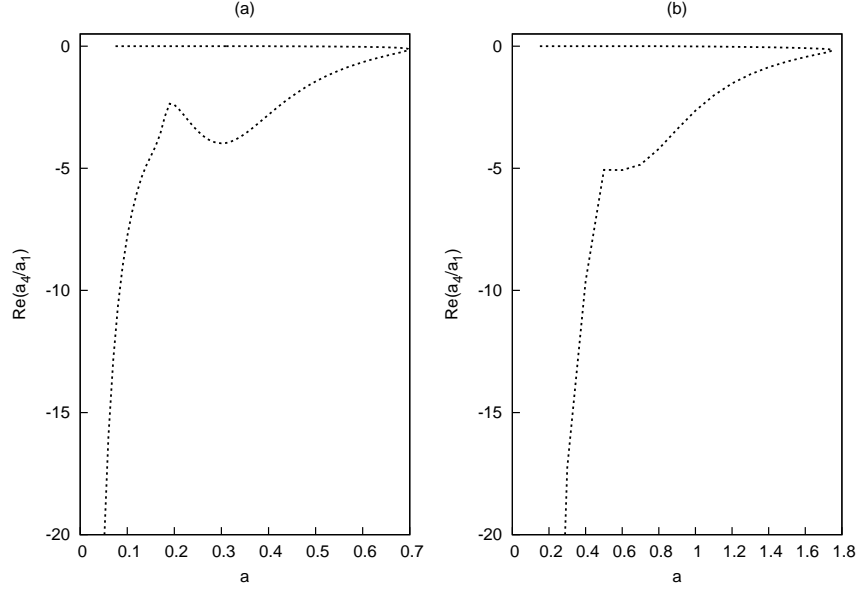


Figure 24: $\text{Re}(a_4/a_1)$ as a function of local cone radius a in the absence of shock. Results are shown for solid wall with (a) $n = 1$ and (b) $n = 2$.

only possible for a finite range of a (see [4]). If no shock is present, solutions to the upper-deck equations at first order are only proportional to $K_n(i\alpha r)$, allowing only for outgoing waves as $r \rightarrow \infty$. This modifies the resulting eigenrelation. The nonlinear stability analysis can be carried out in a straightforward manner for this problem. Figure 24 shows $\text{Re}(a_4/a_1)$ as a function of a for $n = 1$ and $n = 2$. It can be seen that the sign of $\text{Re}(a_4/a_1)$ is always negative and two solution branches exist for $0 < a < 0.75$ for $n = 1$ and $0 < a < 1.75$ for $n = 2$. Thus in the absence of shock nonlinear effects are stabilising for all admissible values of a .

8.3 Effect of porous walls

We can now investigate the effect of porous coatings. We begin by considering the regular porous wall model of (6). The results using the regular microstructure model comprising a regular array of cylindrical pores of circular cross-section are compared to the results for a solid wall for non-axisymmetric modes. The flow conditions match the experimental conditions of [15]. The porous parameters are pore radius $r_p^* = 28.5\mu\text{m}$, porosity $\phi_0 = 0.2$ and pore depth $h^* = 450\mu\text{m}$. Neutral results for $n = 1$ were presented in figure 3a which showed that the porous wall reduces the neutral values of Ω . The porous wall has only a small effect on the neutral values of α (not shown). The difference between the neutral curves of the solid and porous walls is smaller for $n = 2$ compared to $n = 1$ especially for the lower neutral curves. To investigate the effect of nonlinearity we turn to figure 25 which

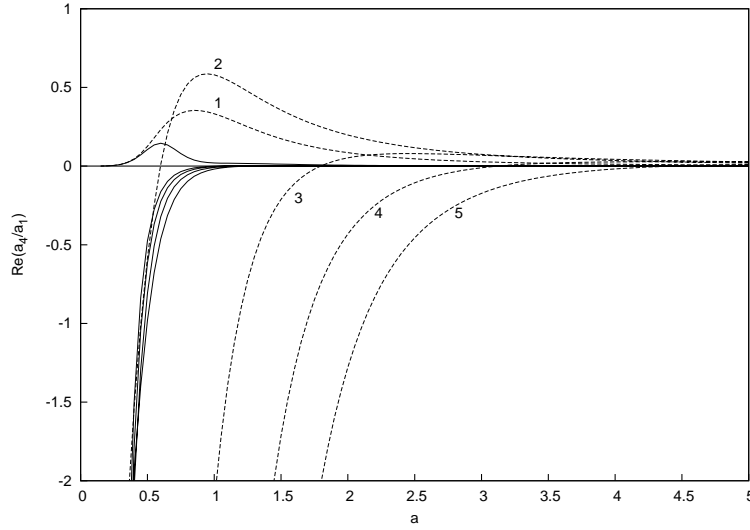


Figure 25: $\text{Re}(a_4/a_1)$ for the first five modes as a function of local cone radius a for $n = 1$ and $a/r_s = 0.57$: —, solid wall; — —, regular microstructure model (6).

compares $\text{Re}(a_4/a_1)$ for $n = 1$ between the solid and regular porous walls for the first five modes ($m = 1, 5$). We see that nonlinear effects are enhanced by the porous wall giving larger values of $\text{Re}(a_4/a_1)$. In the presence of the porous wall nonlinear effects destabilise the lower modes (first and second) while stabilising the higher modes (three to five). We can see this from the fact that $\text{Re}(a_4/a_1)$ for the porous wall has larger positive values for the first and second modes compared to the solid wall and that $\text{Re}(a_4/a_1)$ for the porous wall becomes positive at larger values of a compared with the solid wall for the higher modes. However once destabilised, the higher modes of the porous wall have larger values of $\text{Re}(a_4/a_1)$ compared to the solid wall. For large enough values of a , we can expect the nonlinear effects to diminish just as in the solid wall case. Figure 26 shows the corresponding results for $\text{Re}(a_4/a_1)$ with $n = 2$. Here we see that nonlinearity destabilises the first, second, third and fourth modes in comparison to corresponding modes of the solid wall, while stabilising the fifth and possibly higher modes of the porous wall. Results obtained for $n = 3$ (not shown) show that nonlinearity destabilizes all of the first five modes of the porous wall compared to the solid wall. We can thus infer that in presence of the porous wall, nonlinearity destabilizes lower modes with their mode number increasing with azimuthal wavenumber.

We now compare the effect of porosity on the nonlinear stability of axisymmetric disturbances. We look at figure 27 which shows $\text{Re}(a_{40}/a_{10})$ as a function of a for the porous wall and solid wall. Here we see that in the presence of porous wall all the modes are destabilised by nonlinearity with the most significant effect being felt by the first mode. This mode is destabilised for all values of a .

Next we consider the random microstructure model of (11). The results using this model are compared with those obtained using the regular microstructure model. The porosity of

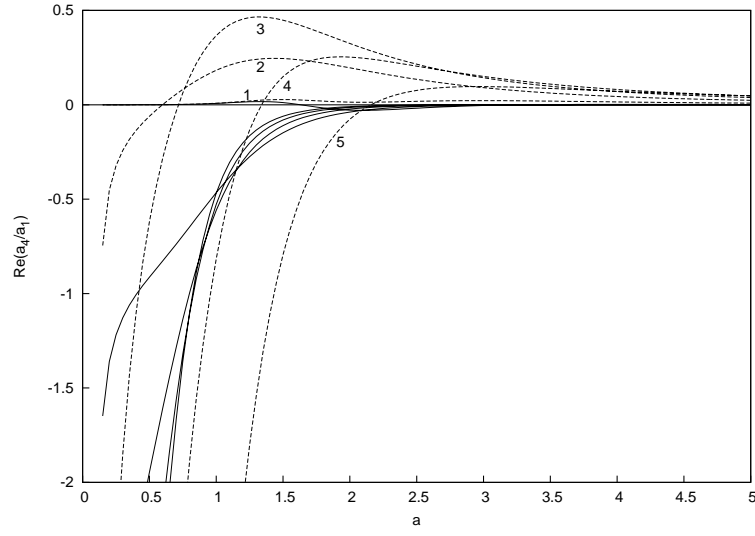


Figure 26: $\text{Re}(a_4/a_1)$ for the first five modes as a function of local cone radius a for $n = 2$ and $a/r_s = 0.57$: —, solid wall; ---, regular microstructure model (6).

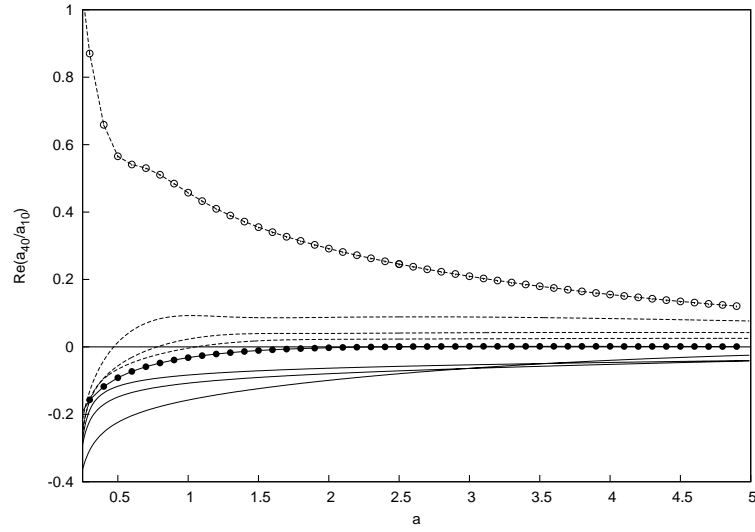


Figure 27: $\text{Re}(a_{40}/a_{10})$ for the first four modes as a function of local cone radius a for $n = 0$ and $a/r_s = 0.57$: —, solid wall; ---, regular microstructure model (6). Results for the first mode are indicated by • for solid wall and ◦ for porous wall.

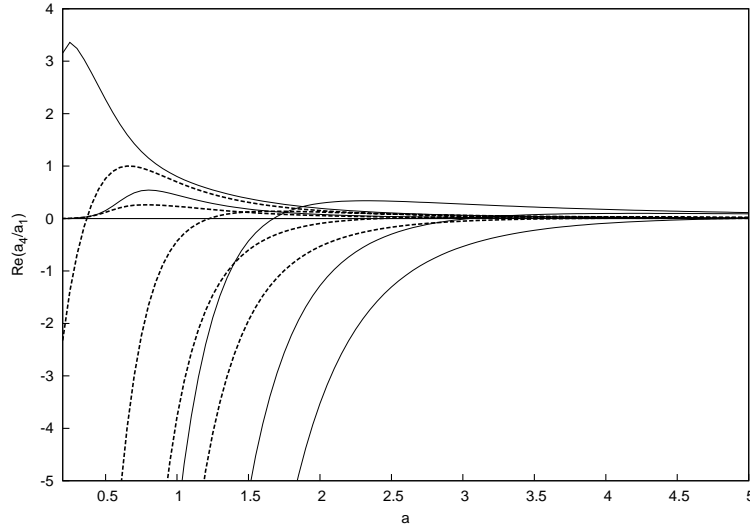


Figure 28: $\text{Re}(a_4/a_1)$ for the first five modes as a function of local cone radius a for $n = 1$ and $a/r_s = 0.57$: —, random microstructure model (11); — —, regular microstructure model (6).

the felt metal is taken to be 0.75 and the fibre diameter is $30\mu\text{m}$. For comparison the regular microstructure model is used with a porosity of 0.2 and pore radius of $30\mu\text{m}$. Figure 28 shows $\text{Re}(a_4/a_1)$ for $n = 1$ for both the models. We see that nonlinear effects destabilise the first two modes of the felt metal model when compared to the regular porous model. The effect on the higher modes is opposite as we see that $\text{Re}(a_4/a_1)$ becomes positive for smaller values of a for the regular porous model as compared to the felt metal model. Once destabilized, values of $\text{Re}(a_4/a_1)$ are more positive for the felt metal indicating that nonlinear amplification of disturbances will be stronger. Similar trends are also observed (not shown) for the case of axisymmetric disturbances.

Finally we consider the mesh microstructure model of (8). The results using this model are compared with those obtained using the regular microstructure model. The porosity of the mesh model is 0.8, and width of each pore section is $100\mu\text{m}$. For comparison the regular porous model is used with a porosity of 0.2 and pore radius of $30\mu\text{m}$. Figure 29 shows $\text{Re}(a_4/a_1)$ for $n = 1$ for both the models. The effect of the two models on the first mode is similar with the destabilising effects of nonlinearity being stronger for the mesh model compared to the regular model. For the higher modes nonlinear effects are slightly more destabilising for the regular model compared to the mesh model. This can again be seen by noting that $\text{Re}(a_4/a_1)$ becomes positive for smaller values of a for the regular model compared to the mesh model. At large values of a , $\text{Re}(a_4/a_1)$ is more positive for the mesh model for the first four modes while for the fifth and possibly higher modes the $\text{Re}(a_4/a_1)$ is larger for the regular model. Corresponding results for axisymmetric disturbances (not shown) indicate no discernible difference between the effects of the two models.

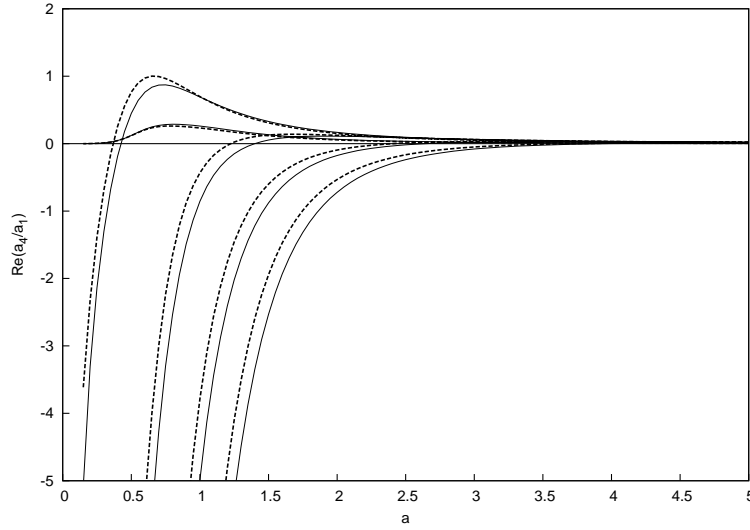


Figure 29: $\text{Re}(a_4/a_1)$ for the first five modes as a function of local cone radius a for $n = 1$ and $a/r_s = 0.57$: —, mesh microstructure model (8); ---, regular microstructure model (6).

9 Discussion and conclusions

We have presented neutral results for the wavenumber and frequency of linear disturbances for hypersonic flow over a passive porous wall, with scales appropriate to the first instability mode for axisymmetric and non-axisymmetric disturbances. The porous wall parameters were chosen to correspond to previous theoretical and numerical studies. For the values chosen here we find that the neutral values of streamwise wavenumber α are slightly reduced from those corresponding to a solid wall. However, the neutral values of the disturbance frequency Ω for non-axisymmetric disturbances can be substantially lower than those for a solid wall, particularly for larger values of radius a . In addition, the spatial growth rates presented demonstrate that the porous wall has a destabilising effect on the axisymmetric and non-axisymmetric modes. The growth rates are significantly larger than those for the solid wall.

The effect of rarefaction for a regular microstructure was shown to be destabilising. This has been shown by [7] to give larger first mode destabilisation and less second mode stabilisation for hypersonic flow over a flat plate.

We have also investigated the effect of the porous wall parameters on the maximum spatial growth rate. The effect of porosity, pore radius and pore depth on the maximum spatial growth rates was also considered. It was shown that increasing each of these quantities leads to larger growth rates, but they level off.

We have made some comparisons of the dimensional growth rates for the first mode disturbances enhanced by the porous surface with those obtained from previous numerical

results for the second mode. It was found that the first mode growth rates were smaller than the second mode ones.

We have determined the effect of regular microstructures, random microstructures and mesh microstructures on the first Mack mode in a hypersonic boundary layer. Our formulation will allow for alternative porous walls to be investigated in a straight-forward manner.

The linear stability analysis presented will not be valid for larger disturbances. Thus, it is important to determine the effect of nonlinearity on the stability of hypersonic boundary layer flow over a sharp slender cone with a porous wall. This has been investigated experimentally for second mode disturbances using the bicoherence method in [16] and [17].

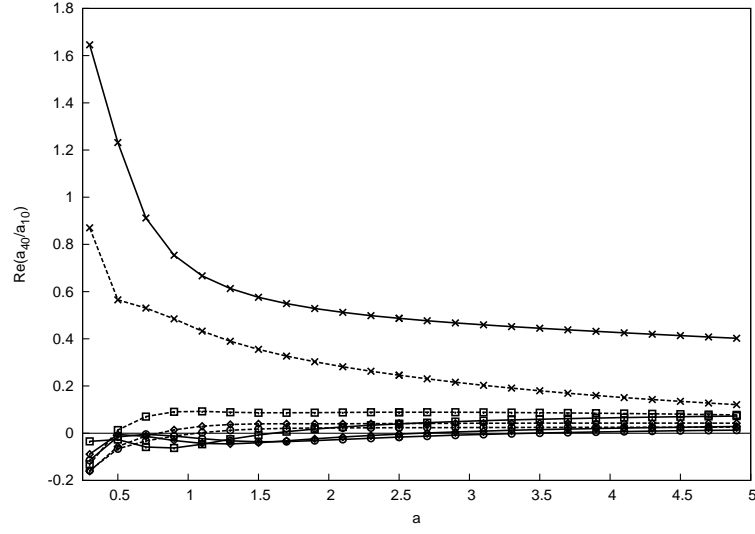
The weakly nonlinear stability of Mack's first-mode disturbances in the hypersonic boundary layer on a sharp slender cone with passive porous walls has been investigated. The effect of the attached shock is found to be significant. In the absence of shock, unstable solutions are possible only for a finite range of cone radius a and nonlinearity stabilises linearly unstable disturbances for all admissible values of a . The presence of the shock leads to multiple unstable modes for all values of a . The effect of nonlinearity is dependent on the mode number and cone radius a . For axisymmetric disturbances on a solid wall, nonlinear effects tend to stabilise all higher modes while the lowest mode is slightly destabilised when a becomes large enough. In the presence of the porous wall all the modes are destabilised when compared to the solid wall. Linear stability results show that the lowest mode is the most unstable and has largest spatial growth rates for both solid and porous walls. This most dangerous mode is also the most destabilized by nonlinearity in the presence of the porous wall. For non-axisymmetric disturbances on a solid wall, nonlinear effects destabilise the lowest mode, while the higher modes are stabilised until a certain value of a which increases with azimuthal wavenumber. All porous wall models destabilise the neutral modes. When considering the effect of nonlinearity on linearly unstable modes, we can state that lower modes are greatly destabilised by nonlinearity while it has a stabilising effect on the higher modes. We have shown that it is the higher modes that have the largest spatial growth rates in the presence of the porous wall. The effect of nonlinearity is to stabilize these most linearly amplified modes by pushing the point of subcritical instability to larger values of a .

The random microstructure felt metal model was compared with the regular porous model. The felt metal significantly destabilizes the neutral modes and strongly amplifies the linearly unstable modes with the higher modes giving the largest growth rates. Nonlinear effects in the presence of the felt metal wall stabilize these more dangerous higher modes over a larger range of a while destabilizing the more slowly growing lower modes. When comparing the difference between the mesh microstructure model and the regular porous model, we notice similar effects between both models on all the modes. The regular porous model slightly destabilises all modes when compared to the mesh model. Since the felt metal and mesh coating have higher porosity, to corroborate these findings, nonlinear stability results for the regular porous model with a higher porosity of $\phi_0 = \frac{\pi}{4}$ were obtained. In figures 30a and 30b for $n = 0$ and $n = 1$, respectively we see that higher porosity leads to nonlinearity having a stabilizing effect on mode numbers greater than one. This is a result of the increase in the value of a where $\text{Re}(a_4/a_1)$ becomes positive. However, for large values

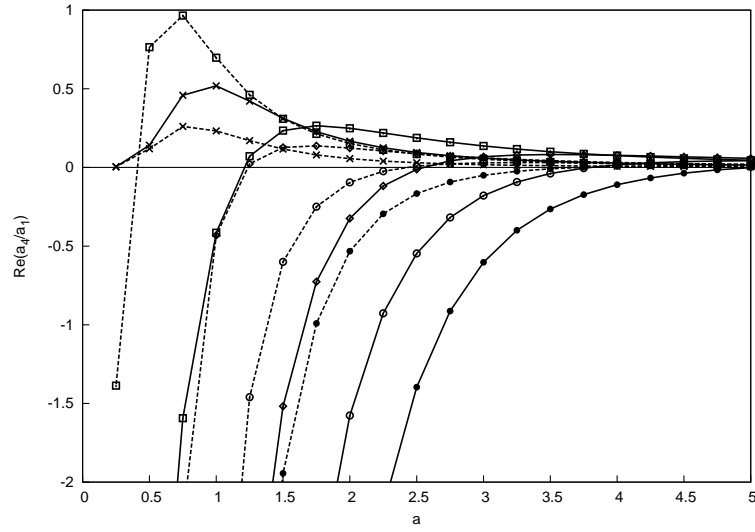
of a the destabilising effect of nonlinearity is stronger with $\text{Re}(a_4/a_1)$ being slightly larger for higher porosity. In figure 31a for $n = 2$ we see the stabilising effect for mode numbers greater than two and in figure 31b for $n = 3$ we see it for mode numbers greater than three. Thus porous coatings with higher porosity allows nonlinear effects to stabilise higher mode number disturbances at a particular location with the mode number of the lowest mode that is stabilised increasing with increasing azimuthal wavenumber.

We can deduce the significance of curvature on the nonlinear stability by comparing our results for a solid wall to those obtained from the analysis of [18] for the weakly nonlinear stability of flow over a wedge. Figure 32 shows the variation of the $\text{Re}(a_3)$, the coefficient of the nonlinear term of the amplitude equation in their paper (cf. equation 5.1) with β_1 , the leading order scaled spanwise wavenumber. The results are shown for a scaled shock distance $\bar{y}_s = 1.73$ which corresponds to the shock angle expected from the flow conditions considered in this paper. Corresponding results (cf. figure 5) shown in [18] were obtained using incorrect values for two constants in their equation 4.12. Our corrected results shows the significant result that for a small range of $0 \leq \beta_1 \leq 0.7$, $\text{Re}(a_3) > 0$. Thus nonlinear effects will be destabilizing for disturbances with these spanwise wavenumbers. By comparing the magnitudes of $\text{Re}(a_3)$ and $\text{Re}(a_4/a_1)$ we can infer that curvature has the effect of making the nonlinear effects stronger.

We now discuss the implications of our results for transition to turbulence. The weakly nonlinear analysis carried out here shows that in the presence of porous walls, lower-frequency first Mack modes are destabilised by nonlinearity while higher-frequency first Mack modes that are destabilised on the solid wall at a particular location now become stabilised for a range of a . This effect is enhanced by models with higher porosity. The porous walls amplify unstable growth rates of the lower-frequency modes when compared to the solid wall. These faster growing modes are further amplified by nonlinearity and may contribute to the early breakdown of laminar flow. Bicoherence diagrams from the experimental investigation of [22] show that in the low-frequency range ($f_1, f_2 < 100\text{kHz}$) nonlinear processes proceed more intensely on the porous wall compared to the solid. The authors suggest that this may be caused by the growth of the low-frequency disturbance amplitudes due to surface roughness. Bicoherence measurements of [16] have also identified a nonlinear interaction that is associated with the destabilised first Mack mode. The authors however state that the nonlinear interaction is too weak to adversely affect the performance of porous walls. These authors only considered measurements from the maximum mass-flow fluctuation location while in [22] measurements were taken throughout the entire thickness of the boundary layer. As the porous wall weakens resonant interactions in the maximum fluctuation layer, [23] show that nonlinear interactions above and below the layer start to play a major role. Nonlinear interaction between vortex (first-mode) waves and filling of the low-frequency vortex-mode spectrum in the presence of porous walls have also been found by theoretical analysis of Gaponov and Terekhova [24]. Simulations by De Tullio & Sandham [25] of transition over a flat plate in the presence of oblique first Mack mode show that the first-mode grows faster than second Mack modes and drives the flow directly to a turbulent state by nonlinear interactions similar to the oblique-transition scenario found at supersonic Mach numbers (see [26] and [27]). De Tullio and Sandham [25] state that the first mode regains

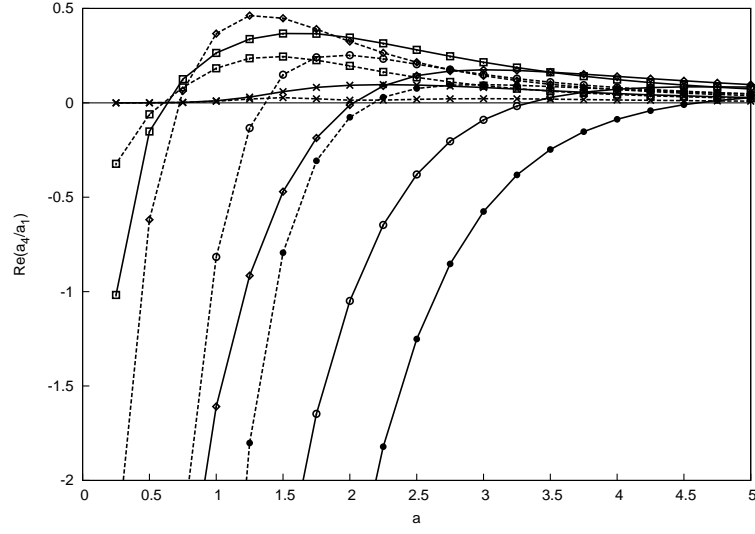


(a)

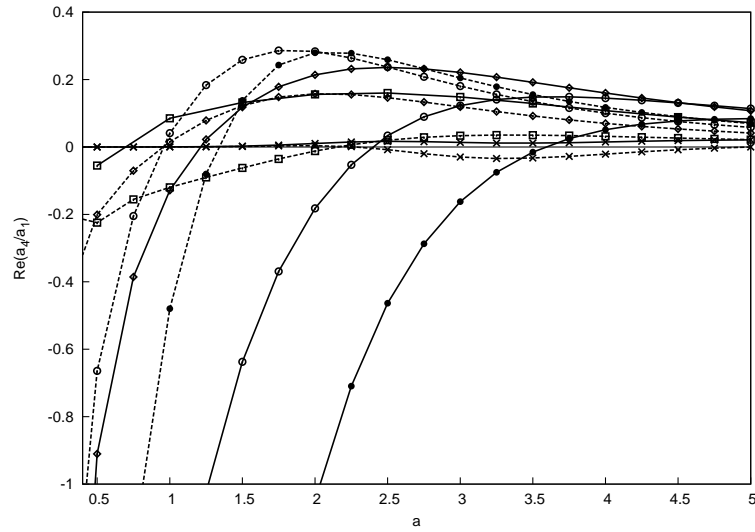


(b)

Figure 30: $\text{Re}(a_4/a_1)$ as a function of local cone radius a for $a/r_s = 0.57$ and (a) $n = 0$; (b) $n = 1$. Results are shown using the regular microstructure model (6): —, $\phi_0 = \pi/4$; ---, $\phi_0 = 0.2$. Symbols refer to mode number: \times , $m = 1$; \square , $m = 2$; \diamond , $m = 3$; \circ , $m = 4$; \bullet , $m = 5$.



(a)



(b)

Figure 31: $\text{Re}(a_4/a_1)$ as a function of local cone radius a for $a/r_s = 0.57$ and (a) $n = 2$; (b) $n = 3$. Results are shown using the regular microstructure model (6): —, $\phi_0 = \pi/4$; ---, $\phi_0 = 0.2$. Symbols refer to mode number: \times , $m = 1$; \square , $m = 2$; \diamond , $m = 3$; \circ , $m = 4$; \bullet , $m = 5$.

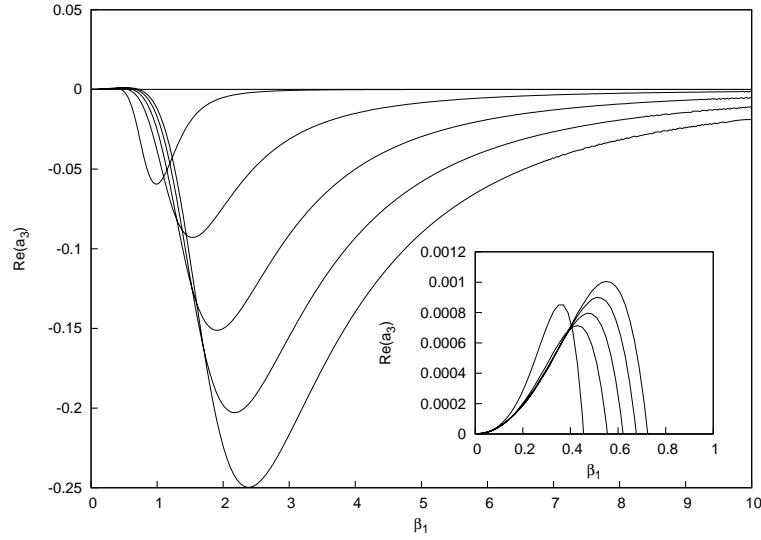


Figure 32: $\text{Re}(a_3)$ for the first five modes as a function of spanwise wavenumber β_1 for $\bar{y}_s = 1.73$ (cf. equation 5.1 of Seddougui & Bassom 1994).

importance in the transition process at high Mach numbers for porous surfaces. The results of the studies reviewed here qualitatively support the conclusions of our analysis that the presence of porous coatings affects the instability of viscous first-mode disturbances leading to significant nonlinear development of disturbances in the low-frequency spectrum.

From this discussion it is clear that further research is required to establish whether Mack's first mode instability can cause transition to turbulence in the presence of porous walls. The work presented here should be extended to consider resonant interactions between the unstable modes identified in this study and its harmonics.

Since it has been observed experimentally and confirmed theoretically and numerically that a porous microstructure destabilises the first Mack mode, it would be desirable to design a microstructure which stabilises the second Mack mode while not appreciably destabilising the first Mack mode. In their efforts to determine types of microstructure which will lead to reduced amplification of the first Mack mode, Wang and Zhong [28] investigated the effect of the phase angle of the wall admittance on the growth of the first Mack mode. For their numerical investigations on a flat plate they discovered that a smaller phase angle of the wall admittance leads to a weaker destabilisation of the first Mack mode. The effect of wall admittance was also investigated theoretically by Carpenter and Porter [29]. They considered a thin porous sheet stretched over a plenum chamber. When the phase of the wall admittance was very close to $\pi/2$ they discovered that Tollmien-Schlichting waves were completely stabilised. Thus, future studies should be focused on determining the wall parameters which will minimise the destabilising effect of a porous wall on the first Mack mode. This will enhance the current knowledge of how the first Mack mode in hypersonic boundary layers may be controlled. It is hoped that such studies will provide optimum design of porous

coatings for incorporation into thermal protection systems as effective techniques for laminar flow control in hypersonic flight vehicles.

References

1. A. V. Fedorov, N. D. Malmuth, A. Rasheed and H. G. Hornung, Stabilization of hypersonic boundary layers by porous coatings, *AIAA J.* **39** (2001) 605–610.
2. A. Fedorov, A. Shipluk, A. Maslov, E. Burov, and N. Malmuth, Stabilization of a hypersonic boundary layer using an ultrasonically absorptive coating, *J. Fluid Mech.* **479** (2003) 99–124.
3. A. Fedorov, V. Kozlov, A. Shipluk, A. Maslov and N. Malmuth, Stability of hypersonic boundary layer on porous wall with regular microstructure, *AIAA J.* **44** (2006) 1866–1871.
4. S. O. Seddougui and A. P. Bassom, Instability of hypersonic flow over a cone, *J. Fluid Mech.* **345** (1997) 383–411.
5. S. O. Stephen, Nonlinear instability of hypersonic flow over a cone, *Q. Jl Mech. Appl. Math.* **59** (2006) 301–319.
6. S. V. Lukashevich, A. A. Maslov, A. N. Shipluk, A. V. Fedorov and V. G. Soudakov, Stabilization of high-speed boundary layer using porous coatings of various thicknesses, AIAA Paper 2010-4720 (2010).
7. X. Wang and X. Zhong, The impact of porous surface on hypersonic boundary layer instability, AIAA Paper 2010-5021 (2010).
8. M. Rasmussen, *Hypersonic Flow*, John Wiley and Sons (1994).
9. W. D. Hayes and R. F. Probstein, *Hypersonic Flow Theory*, Academic (1966).
10. V. F. Kozlov, A. V. Fedorov and N. Malmuth, Acoustic properties of rarified gases inside pores of simple geometries, *J. Acoust. Soc. Am.* **117** (2005) 3402–3412.
11. S. J. Cowley and P. Hall, On the instability of the hypersonic flow past a wedge, *J. Fluid Mech.* **214** (1990) 17–42.
12. P. W. Duck and P. Hall, Non-axisymmetric viscous lower-branch modes in axisymmetric supersonic flows, *J. Fluid Mech.* **213** (1990) 191–201.
13. S. O. Seddougui, Stability of hypersonic flow over a cone. In *Transition, Turbulence and Combustion* (eds. M. Y. Hussaini, T. B. Gatski & T. L. Jackson), pp. 50–59. Kluwer (1994).
14. P. W. Duck and P. Hall, On the interaction of Tollmien–Schlichting waves in axisymmetric supersonic flows, *Q. J. Mech. Appl. Maths* **42** (1989), 115–130.
15. A. A. Maslov, Experimental and theoretical studies of hypersonic laminar flow control using ultrasonically absorptive coatings (UAC), Report ISTC 2172-2001, May 2003.
16. N. Chokani, D. A. Bountin, N. Shipluk, and A. A. Maslov, Nonlinear aspects of hypersonic boundary-layer stability on a porous surface, *AIAA J.*, Vol. 43, No. 1 (2005) 149–155.

17. D. Bountin, A. Shiplyuk, and A. Maslov, Evolution of nonlinear processes in a hypersonic boundary layer on a sharp cone, *J. Fluid Mech.* **611** (2008) 427–442.
18. S. O. Seddougui and A. P. Bassom, Nonlinear instability of hypersonic flow past a wedge, *Q. J. Mech. Appl. Math.* **47** (1994) 557–582.
19. F. T. Smith, Nonlinear stability of boundary layers for disturbances of various sizes, *Proc. R. Soc. A*, **368** (1979) 573–589 (see also A **371** (1980) 439–440).
20. P. Hall and F. T. Smith, A suggested mechanism for nonlinear wall roughness effects on high Reynolds number flow stability, *Stud. Appl. Math.* **66** (1982) 241–265.
21. J. T. Stuart, On the non-linear mechanics of wave disturbances in stable and unstable parallel flows, *J. Fluid Mech.* **9** (1960) 353–370.
22. D. Bountin, A. Maslov, T. Chimytov and A. Shiplyuk, Bispectral analysis of nonlinear processes in the hypersonic boundary layer on a porous cone surface, *Fluid Dyn.* **45** (2010) 415–421.
23. A. A. Maslov, T. Poplavskaya and D. A. Bountin, Hypersonic boundary layer transition and control. In *Seventh IUTAM Symposium on Laminar-Turbulent Transition* (ed. P. Schlatter and D. Henningson), (2010) 19–26. Springer.
24. A. A. Gaponov and N. M. Terekhova, Three-wave interactions between disturbances in the hypersonic boundary layer on impermeable and porous surfaces, *Fluid Dyn.* **44** (2009) 362–371.
25. N. De Tullio and N. D. Sandham, Direct numerical simulation of breakdown to turbulence in a Mach 6 boundary layer over a porous surface, *Phys. Fluids* **22**, (2010) 094105-15.
26. A. D. Kosinov, A. A. Maslov and S. G. Shevelkov, Experiments on the stability of supersonic laminar boundary layers, *J. Fluid Mech.* **219** (1990) 621–633.
27. N. D. Sandham and N. A. Adams, Numerical simulation of boundary-layer transition at Mach two, *Appl. Sci. Res.* **51**, (1993) 371–375.
28. X. Wang and X. Zhong, Phase angle of porous coating admittance and its effect on boundary-layer stabilization, AIAA Paper 2011-3080 (2011).
29. P. W. Carpenter and L. J. Porter, Effects of passive porous walls on boundary-layer instability, *AIAA Journal*, **39** (2001) 597–604.

Appendix A

The complex constants in the amplitude equation (16) involve the following expressions, where as defined in [19]

$$K(\xi) = \text{Ai}(\xi) - \frac{\text{Ai}'(\xi_0)}{L'(\xi_0)} L(\xi), \quad (21a)$$

where

$$L(\xi) = \text{Ai}(\xi) \int_{\xi_0}^{\xi} \frac{ds}{\text{Ai}^2(s)} \int_{\infty}^s \text{Ai}(q) dq, \quad (21b)$$

$$f^{**}(\xi) = i^{1/3} (\text{Ai}(\xi))^{(c)} \left\{ \mathbb{P}_1 \overline{A_Y} \text{Ai}(\xi_0) + \text{Ai}'(\xi) - \text{Ai}'(\xi_0) - \xi \int_{\xi_0}^{\xi} \text{Ai}(t) dt \right\} + c.c.,$$

$$H(\xi) = (i\alpha)^{1/3} \left(F_p(\xi) + \text{Ai}'(\xi) \left(\int_{\xi_0}^{\xi} \text{Ai}(t) dt \right) \right),$$

and $\bar{H} = (i\alpha)^{-1/3} H$. Here

$$F_p(\xi) = \text{Ai}(\hat{\xi}) \int_{\hat{\xi}_0}^{\hat{\xi}} \frac{dq}{\text{Ai}^2(q)} \int_{\infty}^q \text{Ai}(q_2) R(q_2) dq_2,$$

where

$$R(\hat{\xi}) = -2^{-2/3} [2\text{Ai}(\xi)\text{Ai}''(\xi) + (1 - \overline{A_Y}\mathbb{P}_1)\text{Ai}'(\xi_0)\text{Ai}'(\xi)].$$

$$T1 = i^{-1/3} \int_{\xi_0}^{\infty} \left[K(\xi) + K'(\xi)(\xi - \xi_0) \right] \left(\int_{\xi_0}^{\xi} \text{Ai}(s) ds \right) d\xi,$$

$$T3 = -i^{-1/3} \text{Ai}(\xi_0) \text{Ai}'(\xi_0),$$

$$T6 = -i^{1/3} \int_{\xi_0}^{\infty} K'(\xi) \left(\int_{\xi_0}^{\xi} \text{Ai}(s) ds \right) \left(\int_{\xi_0}^{\xi} \left(\int_{\infty}^{\xi_1} f^{**}(t) dt \right) d\xi_1 \right) d\xi,$$

$$T7 = i^{1/3} \left[\frac{dH(\xi)}{d\xi} \right]_{\xi=\xi_0},$$

$$T8 = -i^{4/3} \int_{\xi_0}^{\infty} K'(\xi) \left(\int_{\xi_0}^{\xi} H(t) dt \right) \left(\int_{\xi_0}^{\xi} \text{Ai}(s) ds \right)^{(c)} d\xi,$$

$$T10 = i^{2/3} \int_{\xi_0}^{\infty} K'(\xi) \left(\int_{\xi_0}^{\xi} \left(\int_{\xi_0}^t H(s) ds \right) dt \right) \left(\text{Ai}'(\xi) \right)^{(c)} d\xi,$$

$$T11 = i^{1/3} \int_{\xi_0}^{\infty} K'(\xi) \left(\int_{\xi_0}^{\xi} \left(\int_{\xi_0}^t \text{Ai}(2^{1/3}s) ds \right) dt \right) \left(\text{Ai}(\xi) \right)^{(c)} d\xi,$$

$$T12 = 2i^{2/3} \int_{\xi_0}^{\infty} \bar{H}(t) dt,$$

$$T13 = 2^{2/3} i^{1/3} \int_{\hat{\xi}_0}^{\infty} \text{Ai}(s) ds,$$

$$T14 = -2^{1/3} \frac{d}{d\hat{\xi}} [\text{Ai}(\hat{\xi})]_{\hat{\xi}=\hat{\xi}_0},$$

$$T15 = i^{1/3} \int_{\xi_0}^{\infty} K'(\xi) \left(\text{Ai}'(\xi) - \text{Ai}'(\xi_0) - \xi \left(\int_{\xi_0}^{\xi} \text{Ai}(s) ds \right) \right) \left(\int_{\infty}^{\xi_1} f^{**}(t) dt \right) d\xi,$$

$$T16 = \int_{\xi_0}^{\infty} K'(\xi) \left(\text{Ai}'(\xi) - \text{Ai}'(\xi_0) - \xi \left(\int_{\xi_0}^{\xi} \text{Ai}(s) ds \right) \right)^{(c)} H(\xi) d\xi,$$

$$T17 = i^{-1/3} \int_{\xi_0}^{\infty} K'(\xi) \left(\text{Ai}'(\xi) - \text{Ai}'(\xi_0) - \xi \left(\int_{\xi_0}^{\xi} \text{Ai}(s) ds \right) \right)^{(c)} \text{Ai}(2^{1/3}\xi) d\xi,$$

$$T18 = \int_{\xi_0}^{\infty} K'(\xi) \left(\int_{\xi_0}^{\xi} \text{Ai}(s) ds \right) d\xi,$$

$$\begin{aligned}
T20 &= T6 + T8 + 2T10 - T15 - T16, \\
T21 &= T9 + 2T11 - T17, \\
T22 &= i \int_{\xi_o}^{\infty} K'(\xi) \left(\int_{\infty}^{\xi_1} f^{**}(t) dt \right) \text{Ai}'(\xi_0) d\xi, \\
T23 &= \int_{\xi_o}^{\infty} K'(\xi) \bar{H}(\xi) \text{Ai}'(\xi_0)^{(c)} d\xi, \\
T24 &= i^{-1/3} \int_{\xi_o}^{\infty} K'(\xi) \text{Ai}(2^{1/3}\xi) \text{Ai}'(\xi_0)^{(c)} d\xi, \\
T25 &= i \int_{\xi_o}^{\infty} K'(\xi) \text{Ai}(\xi)^{(c)} d\xi, \\
L2 &= -iT1\kappa^{-1} - 2i^{2/3} \text{Ai}(\xi_0) \text{Ai}'(\xi_0) \kappa^{-1}, \\
L9 &= \left\{ 2 \frac{in^2}{\alpha^{2/3} a^2} g_{2n} T13 - T14 + \{ \alpha^{1/3} g_{2n} T13 \} \overline{A_Y} \right\}^{-1}, \\
L10 &= \left\{ T7 + 2 \frac{in^2}{\alpha^{2/3} a^2} g_{2n} T12 + \left[\alpha^{1/3} g_{2n} T12 + T2 \frac{g_n}{2} \right] \overline{A_Y} \right\}, \\
L11 &= T20 - T21 L9 L10, \\
L12 &= \alpha^{-4/3} T14 L9 L10 + \alpha^{-4/3} T7 - \overline{A_Y} \mathbb{P}_1 T13, \\
L13 &= T23 - T24 L9 L10, \\
L9^0 &= \{ 2i\alpha^{4/3} g_{2n}^0 T13 - T14 + \{ \alpha^{1/3} g_{2n}^0 T13 \} \overline{A_Y} \}^{-1}, \\
L10^0 &= \left\{ T7 + 2i\alpha^{4/3} g_{2n}^0 T12 + \left[\alpha^{1/3} g_{2n}^0 T12 + T2 \frac{g_n^0}{2} \right] \overline{A_Y} \right\}, \\
L11^0 &= T20 - T21 L9^0 L10^0, \\
L12^0 &= \alpha^{-4/3} T14 L9^0 L10^0 + \alpha^{-4/3} T7 - \overline{A_Y} \mathbb{P}_{10} T13, \\
L13^0 &= T23 - T24 L9^0 L10^0, \\
\mathbb{P}_{10} &= (\overline{A_Y} + i\alpha)^{-1}, \\
\mathbb{P}_{20} &= (\overline{A_Y} + 2i\alpha)^{-1}, \\
g_n &= \frac{I_n(i\alpha r_s) K_n(i\alpha a) - I_n(i\alpha a) K_n(i\alpha r_s)}{I_n(i\alpha r_s) K'_n(i\alpha a) - I'_n(i\alpha a) K_n(i\alpha r_s)}, \\
g_{2n} &= \frac{I_{2n}(2i\alpha r_s) K_{2n}(2i\alpha r) - I_{2n}(2i\alpha r) K_{2n}(2i\alpha r_s)}{I'_{2n}(2i\alpha a) K_{2n}(2i\alpha r_s) - I_{2n}(2i\alpha r_s) K'_{2n}(2i\alpha a)}, \\
g_n^0 &= \frac{I_0(i\alpha r_s) K_0(i\alpha r) - I_0(i\alpha r) K_0(i\alpha r_s)}{I_0(i\alpha r_s) K'_0(i\alpha a) - I'_0(i\alpha a) K_0(i\alpha r_s)}, \\
g_{2n}^0 &= \frac{I_0(2i\alpha r_s) K_0(2i\alpha r) - I_0(2i\alpha r) K_0(2i\alpha r_s)}{I_0(2i\alpha r_s) K'_0(2i\alpha a) - I'_0(2i\alpha a) K_0(2i\alpha r_s)}.
\end{aligned}$$

Appendix B

The resulting amplitude equation for axisymmetric disturbances for fixed frequency Ω is

$$a_{10} \frac{dA_{11}}{d\tilde{X}} = a_{20}\lambda_2 A_{11} + a_{40}A_{11}|A_{11}|^2. \quad (22)$$

The coefficients in (22) may be expressed as

$$\begin{aligned} a_{10} = & -i^{4/3} \frac{T1}{\kappa} - 2(i\alpha)^{1/3} \text{Ai}(\xi_0) \alpha \mathbb{P}_{10}^{-1} \\ & \times \left[(b_0 f_0 + c_0 d_0) \left\{ K_0(i\alpha a) - \frac{\text{Ai}'(\xi_0)}{\kappa} (i\alpha)^{-1/3} \mathbb{P}_{10} K_0'(i\alpha a) \right\} \right. \\ & \left. - (b_0 d_0 + c_0 e_0) \left\{ I_0(i\alpha a) - \frac{\text{Ai}'(\xi_0)}{\kappa} (i\alpha)^{-1/3} \mathbb{P}_{10} I_0'(i\alpha a) \right\} \right], \end{aligned} \quad (23)$$

$$a_{20} = i^{-2/3} \alpha L2 + \alpha \kappa^{-1} \overline{A_Y} i^{1/3} T3, \quad (24)$$

$$a_{40} = \frac{i^{-2/3} (\alpha)^{5/3}}{\kappa |\kappa|^2} \left[L11^0 - \overline{A_Y} [\alpha^{2/3} \mathbb{P}_{10} T22 - \mathbb{P}_{20} T25 L12^0] - \overline{A_Y}^{(c)} \mathbb{P}_{10}^{(c)} L13^0 \right], \quad (25)$$

where the corresponding axisymmetric versions of the abbreviations are defined in Appendix A.

List of Symbols, Abbreviations, and Acronyms

a	=	cone radius
\tilde{a}	=	half-pore width
a_∞	=	tortuosity
A	=	displacement function
A_y	=	admittance
$\overline{A_Y}$	=	scaled admittance
C_D	=	$C_D^* \gamma p_-$, dynamic compressibility
d^*	=	fibre diameter
h	=	h^*/δ^* , non-dimensional porous-layer thickness
L^*	=	length scale
Kn	=	Knudsen number
M	=	Mach number
n	=	azimuthal wavenumber
Pr	=	Prandtl number
P	=	pressure disturbance
R	=	$U_- \delta^*/\nu_-$, Reynolds number
Re	=	Reynolds number
r_p	=	r_p^*/δ^* , non-dimensional pore radius
r_s	=	shock location
T	=	temperature
u, v	=	velocity disturbance
U	=	velocity
x, \bar{r}, ϕ	=	orthogonal coordinates
Z_0	=	characteristic impedance
α	=	$\alpha_r + i\alpha_i$, disturbance streamwise wavenumber
δ^*	=	boundary-layer displacement thickness
γ	=	specific heat ratio
θ_c	=	cone angle
θ_s	=	shock angle
λ	=	skin friction
Λ	=	propagation constant
ω	=	angular frequency
Ω	=	frequency
μ	=	viscosity
ν	=	kinematic viscosity
ρ	=	density
ρ_D	=	ρ_D^*/ρ_W^* , dynamic density
ϕ_0	=	porosity
σ^*	=	flow resistivity

Subscripts

— = just behind the shock
 s = shock
 w = wall
0 = initial